Contract No.:

This manuscript has been authored by Savannah River Nuclear Solutions (SRNS), LLC under Contract No. DE-AC09-08SR22470 with the U.S. Department of Energy (DOE) Office of Environmental Management (EM).

SRNL-STI-2021-00062

Simulations of Crack Extensions in Arc-Shaped Tension Specimens of Uncharged and Hydrogen-Charged 21-6-9 Austenitic Stainless Steels Using Cohesive Zone Modeling with Varying Cohesive Parameters

Shin-Jang Sung and Jwo Pan
Mechanical Engineering
University of Michigan
Ann Arbor, MI 48109, USA

Paul S. Korinko and Michael Morgan (Retired)
Savannah River National Laboratory
Aiken, South Carolina, USA

February 2021

Keywords: arc-shaped tension specimen; fracture test; cohesive zone modeling; trapezoidal traction-separation law; varying cohesive parameters; hydrogen effect

For publication in Engineering Fracture Mechanics

Simulations of Crack Extensions in Arc-Shaped Tension Specimens of Uncharged and Hydrogen-Charged 21-6-9 Austenitic Stainless Steels Using Cohesive Zone Modeling with Varying Cohesive Parameters

Shengjia Wu and Jwo Pan[1]
Mechanical Engineering
University of Michigan
Ann Arbor, MI 48109

Paul S. Korinko and Michael J. Morgan
Materials Science and Technology
Savannah River National Laboratory
Aiken, SC 29808

February 4, 2021

Abstract

Crack extensions in uncharged and hydrogen-charged side-grooved A(T) specimens of conventionally forged 21-6-9 austenitic stainless steels are simulated using the cohesive zone modeling approach. Two-dimensional plane strain finite element analyses with fixed cohesive parameters are first conducted to fit the experimental load-displacement curves. Similar analyses using varying cohesive parameters as functions of the crack extension are then conducted to fit the experimental load-crack extension and crack extension-displacement curves. The computational results with varying cohesive parameters can fit very well the experimental data. The computational results also indicate that the average cohesive energy for the hydrogen-charged A(T) specimen is lower than that for the uncharged A(T) specimen.

Keywords: arc-shaped tension specimen; fracture test; cohesive zone modeling; trapezoidal traction-separation law; varying cohesive parameters; hydrogen effect

[1] Corresponding author. Tel.:+1-734-764-9404; fax:+1-734-647-3170

Email address: jwo@umich.edu (Jwo Pan)

Nomenclature

a_0	initial crack length
B	specimen thickness
B_n	net specimen thickness
E	Young's modulus
J	J integral
$J_{0.2}$	J integral determined by blunting line based on ASTM Standard E1820
K , n	material constants of tensile true stress-plastic strain curve
T	traction
T_0	cohesive strength
$\overline{T}_0$	average cohesive strength for varying cohesive strength function
X , Y	Cartesian coordinates
Γ_0	cohesive energy
$\overline{\Gamma}_0$	average cohesive energy for varying cohesive energy function
δ	separation
δ_0	separation at the end of softening of the traction-separation law
δ_1	separation at the end of the rising part of the traction-separation law

δ_2 separation at the initiation of softening of the traction-separation law

δ_2/δ_0 softening ratio of the traction-separation law

Δa crack extension

Δa_f final crack extension measured from experiment

ε_p plastic strain

ν Poisson's ratio

σ true stress

σ_Y yield stress

1. Introduction

The cohesive zone modeling (CZM) approach has been used to model crack extensions in laboratory fracture specimens of ductile materials [1-6]. In order to obtain accurate computational results with the CZM approach for practical applications, the two most important cohesive parameters, cohesive energy and cohesive strength, should be carefully calibrated. Different approaches were used to calibrate the cohesive energy and cohesive strength for the exponential and trapezoidal traction-separation laws for different fracture specimens of different ductile materials, depending on the availability of the experimental load-displacement-crack extension data for the fracture specimens and the experimental data for tensile or notched specimens as, for example, in Roychowdhury et al. [1], Cornec et al. [2], Scheider and Brocks [3, 4], Sung et al. [5], and Wu et al. [6]. In the cohesive zone modeling approach, cohesive parameters are usually assumed as fixed values [1-6]. The CZM approach with fixed cohesive

parameters can be adopted with only two important cohesive parameters, cohesive energy and cohesive strength, to be calibrated.

For a fracture specimen, where the size requirements of the plane strain conditions of the linear elastic fracture mechanics are satisfied at crack initiation and during crack extension, the selection of the cohesive energy can be a fixed value related to the fracture toughness at crack initiation and during crack extension. However, for a cracked thin structure or a fracture specimen cut from the actual applications, the majority of the crack front may not be subjected to the plane strain conditions at crack initiation and during crack extension. Then the cohesive energy should vary to reflect the change from the flat fracture to the slant fracture mode or the change of the constraint conditions due to the change of the plastic zone size and shape along the crack front for a two-dimensional plane stress or plane strain finite element analyses of crack extension with the CZM approach. Schwalbe et al. [7] discussed the possibility of splitting the finite element model for thin cracked structures into two regions where the first region close to crack initiation is governed by the cohesive parameters for a flat crack extension and the second region is governed by the cohesive parameters for a slant crack extension. Simonsen and Tornqvist [8] conducted experiments for crack propagation in large thin fracture specimens of normal strength steel, high strength steel and aluminum A5083 H116 and H321 alloys. Woelke et al. [9] later conducted finite element analyses using the CZM approach with the varying cohesive parameters as functions of the crack extension for crack extension of many thicknesses in the large thin edge-notched specimen of aluminum A5083 H116 of Simonsen and Tornqvist [8]. The width, initial notch length and thickness of the large thin edge-notched specimen are 500 mm, 100 mm and 10 mm, respectively. Woelke et al. [9] used the shell elements with the

element size of 12.7 mm, slightly larger than the specimen thickness, in the finite element analyses to model the crack extension in the thin specimen.

Woelke et al. [9] used the experimental load-displacement curve of Simonsen and Tornqvist [8] to calibrate the varying cohesive parameters and demonstrated the accuracy of the plane stress shell finite element analyses with the cohesive zone modeling of crack extension. The computational load-displacement curve of the large thin specimen from the plane stress shell finite element analysis is in good agreement with the experimental data based on the identified varying cohesive parameters. In Simonsen and Tornqvist [8], the final crack extension in the large thin edge-notched specimen is about 35 times of the specimen thickness. Woelke et al. [9] selected the cohesive energy increased from a lower value close to the one corresponding to the fracture toughness for crack initiation to a large value of the cohesive energy for plane strain tension for the crack extension of about 7 times of the specimen thickness. It should be emphasized again that in Woelke et al. [9], the element size in their shell finite element model is scaled with the specimen thickness and the steady-state cohesive energy is based on the work per unit area under the normalized force-elongation curve for plane strain tension from the onset of necking to the onset of shear localization as presented in Nielsen and Hutchinson [10]. The transition from the low cohesive energy for the initial flat fracture to the high cohesive energy for the slant fracture requires the crack to grow about 7 times of the thickness. The results of the plane stress shell finite element analysis catch the trends of the increasing cohesive energy and cohesive strength for the first shell element with the size of about the specimen thickness for the initial flat fracture supposedly under near plane strain conditions.

Andersen et al. [11] conducted three-dimensional finite element analysis of the crack extension in the same thin edge-notched specimen of Simonsen and Tornqvist [8] based on the

GTN material model (Gurson [12], Tvergaard [13], and Tvergaard and Needleman [14]). The cohesive energy and cohesive strength as functions of the radial distance to the original notched tip were extracted from the results of the three-dimensional finite element analysis. Then, the extracted varying cohesive energy and varying cohesive strength were adopted in two-dimensional plane stress finite element analyses to simulate the crack extension. They found that in order to use the varying cohesive energy and varying cohesive strength in the two-dimensional plane stress finite element analysis to fit the simulation results from the three-dimensional finite element analysis with the GTN material model, some fitting processes such as increases of the cohesive strength and cohesive energy were still needed. However, the fitted varying cohesive strength and varying cohesive energy for the two-dimensional plane stress finite element analysis follow the general trends of those extracted from the results of the three-dimensional finite element analysis with the GTN material model. It should be noted that the transition crack extension corresponding to the varying cohesive strength from a low value to a steady-state value is about 2 times of the specimen thickness and the transition crack extension corresponding to the varying cohesive energy from a low value to a steady-state value is about 7 times of the specimen thickness. Similarly, the results of the two-dimensional plane stress finite element analysis also catch the trends of the increasing cohesive energy and cohesive strength for the first plane stress element with the size of about the specimen thickness for the initial flat fracture supposedly under near plane strain conditions.

For thin structures such as pressure tubes in nuclear reactors, modeling of crack extensions less than the specimen thickness by a two-dimensional finite element analysis with the CZM approach is an important fracture mechanics application. Sung et al. [15] conducted two-dimensional finite element analyses with the varying cohesive energy to simulate the crack

extension in a small thin curved compact tension (CCT) specimen of Zr-2.5Nb pressure tube material. The CCT specimen was cut from an ex-service pressure tube. The width, initial crack length and thickness of the CCT specimen are 17 mm, 8.75 mm and 4.2 mm, respectively. In Sung et al. [15], the final crack extension of 3.88 mm in the as-removed CCT specimen is smaller than the specimen thickness of 4.2 mm. Therefore, the two-dimensional shell or plane stress finite element analyses with the CZM approach of Woelke et al. [9] and Andersen et al. [11] with the crack extension of many thicknesses is not applicable. It should be noted that Sung et al. [16] found that a two-dimensional elastic plane stress finite element analyses of the CCT specimen can be used to model the initial elastic stiffness of the load-displacement curve. Therefore, the CCT specimen can be modeled as a thin plane stress specimen. However, Sung et al. [17] conducted three-dimensional elastic-plastic finite element analyses of the CCT specimen. Their computational results indicated that the majority of the crack front is under plane strain conditions at the maximum load. Therefore, a two-dimensional plane strain finite element analysis to simulate crack extension in the CCT specimen is appropriate to be used with the elastic stiffness adjustment method to account for the initial plane stress load-displacement response of the specimen in Sung et al. [15].

Sung et al. [15] selected the finite element size scaled with the crack tip opening displacement, estimated from the J integral divided by the yield stress, for the simulation of the crack extension in the CCT specimen. The finite element size was selected to catch the maximum opening stress ahead of the crack tip in the two-dimensional plane strain finite element analysis with consideration of the finite deformation of the crack tip under plane strain conditions. Sung et al. [15] selected the maximum opening stress ahead of the initial crack tip as the cohesive strength. Sung et al. [15] selected the bilinear varying cohesive energy as a function

of the crack extension by following the trend of the experimental J-R curve of the specimen. The computational load-displacement curve in Sung et al. [15] can fit the experimental data quite well. Also, the computational load-crack extension, crack extension-displacement and J-R curves can fit the general trends of the experimental data. The increase of the varying cohesive energy, following the trends of the experimental J integrals and the trend of the computational separation work rate [18] (or the negative work to open the crack per unit area), can be used to account for the decrease of the plane strain portion of the crack front from the increase of the plastic zone size as the crack extension increases. The two-dimensional plane strain finite element analysis of the initial flat crack extension with the element size scaled with the crack tip opening displacement cannot be modeled by the shell or plane stress finite element analyses with the element size scaled with the specimen thickness as in Woelke et al. [9] and Andersen et al. [11].

It should be noted that when the constraint conditions decrease for the portion of the crack front due to the effect of the free surfaces, the cohesive energy to extend the entire crack front is higher as shown in Sigmund et al. [19, 20] based on the GTN material model. It should be mentioned that the plane strain conditions of the linear elastic fracture mechanics (LEFM) for the CCT specimen are satisfied at crack initiation. However, after a small amount of crack extension, the plane strain conditions of the LEFM are not satisfied anymore. The increase of the cohesive energy for the entire crack front is due to the higher cohesive energy from the decrease of the constraint conditions for the portion of the crack front close to the free surfaces as the crack extension increases. The results of the two-dimensional plane strain finite element analysis in Sung et al. [15] catch the trends of the increasing cohesive energy for the crack

extension less than the specimen thickness with the element size scaled with the crack tip opening displacement for the initial flat fracture under near plane strain conditions.

For small thin stainless steel specimens with different hydrogen contents, modeling and testing for crack extension less than the specimen thickness is also an important fracture mechanics application. Wu et al. [6] conducted two-dimensional plane strain finite element analyses with the CZM approach to simulate the crack extension in small side-grooved arc-shaped tension A(T) specimens of uncharged and tritium-charged-and-decayed CF 21-6-9 stainless steels. The side grooves were cut to promote the flat fracture. The width and net thickness of the A(T) specimen are 9.22 mm and 3.81 mm, respectively. The initial crack lengths in the A(T) specimens are in the range of 4.32 mm to 5.75 mm. In Wu et al. [6], the final crack extensions are in the range of 1.61 mm to 2.48 mm which are smaller than the net specimen thickness of 3.81 mm. With the side grooves, the two-dimensional plane strain finite element analyses can be used to model the initial elastic stiffnesses of the experimental load-displacement curves of the A(T) specimens. It should be mentioned that the A(T) specimens are small and the size requirements of the J integral testing are not satisfied as discussed in Kim et al. [21].

Wu et al. [6] selected the fixed cohesive parameters based on the deviation load approach by comparing the computational load-displacement curves from the stationary crack model with the experimental data as in Sung et al. [5] for small single edge bend specimens of additively manufactured 304 stainless steels. In Wu et al. [6], the experimental J integrals at the deviation loads of the A(T) specimens were taken as the reference cohesive energies, and the maximum opening stresses ahead of the initial crack tips in the A(T) specimens were taken as the reference cohesive strengths for the uncharged and tritium-charged-and-decayed A(T) specimens to start

the calibration processes. Wu et al. [6] calibrated the fixed cohesive parameters based on fitting the maximum loads of the experimental load-displacement curves. The computational load-displacement curves agreed reasonably well with the experimental data for both uncharged and tritium-charged-and-decayed A(T) specimens. However, the computational load-crack extension and crack extension-displacement curves showed some differences from the experimental data. For example, the computational maximum loads occurred much earlier than the corresponding experimental data.

Sung et al. [22] conducted the two-dimensional plane strain finite element analyses to simulate the crack extensions in the A(T) specimens with the nodal release method. Sung et al. [22] obtained the separation work rates (or the negative work to open the crack per unit crack area) and the maximum opening stresses ahead of crack tips as functions of the crack extension in the A(T) specimens. The computational results indicate that the separation work rates and maximum opening stresses ahead of the crack tips vary as the cracks extend from the original crack tips to the final crack lengths in the small A(T) specimens. The varying separation work rates and maximum opening stresses indicate that the cohesive energy and cohesive strength may vary as the crack extension increases due to the varying constraint conditions along the crack front. It should be mentioned that since the size requirements of the J integral testing are not satisfied for the small A(T) specimens, the cohesive energy may increase as the crack extension increases due to gradual loss of the plane strain conditions along the portions of the crack front from the increase of the plastic zone size.

In this investigation, finite element analyses with fixed cohesive parameters are first conducted to determine the cohesive strengths and cohesive energies to fit the maximum loads of the experimental load-displacement curves of uncharged and hydrogen charged A(T) specimens

of CF 21-6-9 stainless steels. It should be noted that the finite element size near the crack tips for the simulations of crack extensions is scaled with the crack tip opening displacement to catch the maximum opening stresses ahead of the crack tips with consideration of the finite deformation of the crack tips under plane strain conditions as in Sung et al. [22]. The procedures to select the fixed cohesive parameters for uncharged and hydrogen-charged A(T) specimens are similar to that reported in Wu et al. [6] based on the deviation loads and the maximum opening stresses ahead of the initial crack tips determined from the stationary crack models with the initial crack lengths. Next, finite element analyses with varying cohesive parameters are conducted to calibrate the cohesive parameters by following the general trends of the separation work rates and maximum opening stresses ahead of the crack tips in Sung et al. [22] to improve the computational load-crack extension and crack extension-displacement curves for uncharged and hydrogen-charged A(T) specimens. In this investigation, the cohesive energies, cohesive strengths and softening ratios are selected as functions of the crack extension to fit the experimental load-displacement, load-crack extension, and crack extension-displacement curves of uncharged and hydrogen-charged A(T) specimens. The selection processes of the varying cohesive parameters are presented in detail in Appendix A. After the varying cohesive parameters are calibrated for one uncharged A(T) specimen, finite element analyses with the selected varying cohesive parameters are also conducted for two other uncharged A(T) specimens with different initial crack lengths to obtain the computational load-displacement, load-crack extension, crack extension-displacement and J-R curves for comparison with the experimental data in Appendix B. Then, the separation work rate and maximum opening stress ahead of the crack tip in Sung et al. [22] are presented and compared with the selected varying cohesive energy and varying cohesive strength, respectively, for the uncharged A(T) specimen.

The plastic zone sizes and shapes at different crack extensions from crack initiation to a large crack extension under fully plastic conditions for the uncharged A(T) specimen are also presented for a possible connection to the varying cohesive energy. Finally, some conclusions are made.

2. Two-Dimensional Finite Element Models of A(T) Specimens without and with Cohesive Elements

Figure 1 shows schematics of side and front views of an A(T) specimen with side grooves. As shown in the figure, the A(T) specimen has side grooves on the free surfaces. The initial crack length a_0, the specimen thickness B, the net specimen thickness B_n, and the initial crack mouth opening displacement (COD) for the uncharged H94-1, H94-2 and H94-4 and hydrogen-charged H94-54 A(T) specimens from Morgan [23] are listed in Table 1. The hydrogen concentration in the hydrogen-charged H94-54 A(T) specimen was determined to be about 78 ppmw. Kim et al. [21] conducted three-dimensional finite element analyses of a side-grooved A(T) specimen of CF 21-6-9 stainless steel. Their computational results indicated that the crack tip fields along the crack front are near plane strain conditions. Therefore, two-dimensional plane strain finite element analyses without and with cohesive elements are used to select cohesive parameters to fit the experimental data of the uncharged and hydrogen-charged A(T) specimens. The prescribed crack extension paths are straight ahead of the initial crack tips.

Figure 2 shows the finite element model for an A(T) specimen with cohesive elements. The Cartesian $X-Y$ coordinate system is also shown in Figure 2. In the figure, the blue circular regions represent the deformable steel pins. The small central holes in the circular regions are constrained as rigid bodies with the control nodes located at the centers of the holes. The

interfaces between the pins and the pin holes of the A(T) specimen are modeled with the contact definition of no-penetration in the normal direction and no-friction in the tangential direction. For the boundary conditions of the finite element model, an upward displacement is applied to the center of the upper pin and an equal downward displacement is applied to the center of the lower pin. It is possible to model only the upper half or the lower half of the specimen for the finite element analyses without cohesive elements due to symmetry. However, for consistency with the finite element analyses with cohesive elements, the entire specimen is modeled in the finite element analyses without cohesive elements. For the finite element analyses without cohesive elements, no cohesive elements are placed ahead of the initial crack tip. For the finite element analyses with the cohesive elements as shown in Figure 2, the cohesive elements are placed directly ahead of the initial crack tip in the X direction except a small region near the right surface. As shown in Figure 2, the cohesive elements are marked in blue and the small region without cohesive elements near the right surface are marked in yellow. The cohesive elements should not be placed ahead of the initial crack tip in the entire ligament since the continuum elements nearby the cohesive elements near the right surface under compression can have significant overlaps.

The computational crack mouth opening displacements (COD's) are collected from the distances between the locations of two notches as shown in Figure 1. The detailed design of the notches for mounting the clip gauge is not modeled since the region near the mounting notches hardly deforms. The locations to take the initial COD are marked by two red dots in Figure 2. The initial COD's for all A(T) specimens are listed in Table 1 as mentioned earlier. The initial crack length a_0 is marked in red in Figure 2 and the values of the initial crack length a_0 for all A(T) specimens are listed in Table 1. Two-dimensional linear plane strain elements with full

integration (CPE4) are used. The smallest elements of 0.025 mm by 0.025 mm are located near the crack, the ligament and cohesive elements. Other element sizes vary from 0.05 mm by 0.05 mm to 0.5 mm by 0.5 mm. The material definition for the steel loading pin is linear elastic with the Young's modulus of 210 GPa and the Poisson's ratio of 0.3.

The material definitions for the uncharged CF 21-6-9 stainless steels were obtained from a tensile test with a round bar specimen as discussed in Wu et al. [24]. The material definitions for the hydrogen-charged CF 21-6-9 stainless steels follow the estimation procedure in Wu et al. [24] based on the different yield stresses of high-energy-rate-forged (HERF) steels with different hydrogen contents [25]. The Young's modulus E is determined to be 177.33 GPa and the Poisson's ratio ν is assumed to be 0.3. The 0.2% offset yield stress σ_Y is determined to be 856.48 MPa and 867.54 MPa for the uncharged and hydrogen-charged CF steels, respectively. The material constants for the uncharged and hydrogen charged CF 21-6-9 stainless steels are listed in Table 2. Figure 3 shows the true stress-plastic strain curve for the uncharged CF steel (black solid line) based on the initial part of the experimental stress-strain data and the assumed power-law relation for the final part of large plastic strains as presented in Wu et al. [24]. The true stress-plastic strain curve for the hydrogen-charged CF steel (red dashed line) is also shown in Figure 3 based on the estimation procedure as discussed in Wu et al. [24]. The PPR user-defined cohesive element subroutine [26, 27] for ABAQUS is adopted with the smooth trapezoidal traction-separation law [2]. The commercial finite element program ABAQUS was employed to perform the analyses of the A(T) specimens with consideration of geometric nonlinearity.

3. Cohesive Zone Model

The smooth trapezoidal traction-separation law [2-4] was used to simulate crack extensions in finite element analyses of fracture specimens of ductile metals. Figure 4 shows a schematic of the normalized smooth trapezoidal traction-separation law used in this study. The smooth traction-separation law has the initial stiff part so that the initial responses of the experimental load-displacement curves of fracture specimens can be fitted well [2-6]. The smooth traction-separation law consists of three polynomials as

$$T=\begin{cases} T_0\left[2\left(\dfrac{\delta}{\delta_1}\right)-\left(\dfrac{\delta}{\delta_1}\right)^2\right] & 0\le\delta<\delta_1 \\ T_0 & \delta_1\le\delta<\delta_2 \\ T_0\left[2\left(\dfrac{\delta-\delta_2}{\delta_0-\delta_2}\right)^3-3\left(\dfrac{\delta-\delta_2}{\delta_0-\delta_2}\right)^2+1\right] & \delta_2\le\delta<\delta_0 \end{cases} \tag{1}$$

where T is the traction and T_0 is the cohesive strength. The separation is represented by δ. The separation at the end of the initial part of the traction-separation law is represented by δ_1. The separation at the onset of softening is represented by δ_2. The final separation is represented by δ_0 when the traction becomes zero. The cohesive energy Γ_0 is defined as the area under the traction-separation curve. The unit of the cohesive energy Γ_0 is the same as those of the J integral and the separation work rate. It should be noted that δ_1 should be small enough to prevent inducing too much artificial compliance for the fracture specimens as mentioned earlier but large enough to assure computational stability. In this investigation, the ratio δ_1/δ_0 is selected to be 0.005 for all simulations. For $\delta<0$, an elastic response with a large stiffness (500 times of the initial tensile stiffness) is assigned to prevent significant overlap of two adjacent continuum elements.

4. Computational Results Based on Fixed Cohesive Parameters

In this investigation, finite element analyses without cohesive elements are conducted first to estimate the cohesive parameters to fit the maximum loads of the experimental load-displacement curves for uncharged and hydrogen-charged A(T) specimens. The crack initiations are identified at the deviation loads where the computational load-displacement curves of the finite element analyses with the initial crack lengths without cohesive elements start to deviate from the experimental data. Figure 5(a) shows a comparison of the experimental load-displacement curve and the computational load-displacement curve from the finite element analysis without cohesive elements for the uncharged H94-2 specimen. The deviation load is defined as the load at which the computational load-displacement curve (red dashed line) deviates from the experimental load-displacement curve (black solid line). The deviation load of 1,385 N of the uncharged H94-2 specimen is marked in Figure 5(a). The J integral of 30.1 kJ/m^2 at the deviation load is determined from the experimental data. The deviation load and the J integral at the deviation load for the uncharged H94-2 specimen are listed in Table 3. Figure 5(b) shows a comparison of the experimental load-displacement curve and the computational load-displacement curve from the finite element analysis without cohesive elements for the hydrogen-charged H94-54 specimen. The deviation load of 2,717 N of the hydrogen-charged H94-54 specimen is marked in Figure 5(b). The J integral of 23.6 kJ/m^2 at the deviation load is determined from the experimental data. The deviation load and the J integral at the deviation load for the hydrogen-charged H95-54 specimen are also listed in Table 3.

Also, the opening stress distributions ahead of the initial crack tips in the A(T) specimens are determined from the finite element analyses with the initial crack lengths without cohesive elements. Figure 6(a) shows the distribution of the opening stress ahead of the initial crack tip at

the deviation load for the uncharged H94-2 specimen from the finite element analysis without cohesive elements. The maximum value of the distribution of the opening stress ahead of the initial crack tip at the deviation load is 2,619 MPa. Figure 6(b) shows the distribution of the opening stress ahead of the initial crack tip at the deviation load for the hydrogen-charged H94-54 specimen from the finite element analysis without cohesive elements. The maximum value of the distribution of the opening stress ahead of the initial crack tip at the deviation load is 2,814 MPa. The maximum opening stresses for the uncharged H94-2 and hydrogen-charged H94-54 specimens are also listed in Table 3.

The J integrals determined from the experimental data at the deviation loads of the A(T) specimens are taken as the reference cohesive energies and the maximum opening stresses ahead of the initial crack tips in the A(T) specimens determined from the finite element analyses with the initial crack lengths without cohesive elements are taken as the reference cohesive strengths. Then, finite element analyses with cohesive elements are conducted with the cohesive strengths and cohesive energies adjusted to fit the maximum loads of the experimental load-displacement curves of the A(T) specimens. The selected fixed cohesive parameters for the uncharged H94-2 and hydrogen-charged H94-54 A(T) specimens are listed in Table 4. Figure 7 shows the smooth trapezoidal traction-separation laws with the selected fixed cohesive parameters for the uncharged H94-2 and hydrogen-charged H94-54 A(T) specimens. As shown in Figure 7 and listed in Table 4, the cohesive strength for the hydrogen-charged H94-54 specimen is higher than that for the uncharged H94-2 specimen while the cohesive energy (the area under the traction-separation curve) for the hydrogen-charged H94-54 specimen is lower than that for the uncharged H94-2 specimen. Detailed modeling of hydrogen embrittlement and cohesive zone modeling for steels can be found in two review papers [28, 29]. The cohesive zone modeling

approach coupled with hydrogen diffusion as discussed in [29] is not considered in this investigation and is out of the scope of this paper.

The computational load-displacement, load-crack extension, crack extension-displacement and J-R curves with the fixed cohesive parameters for the uncharged H94-2 specimen are compared with the experimental data in Figures 8(a), 8(b), 8(c), and 8(d), respectively. As shown in Figures 8(a) to 8(d), the computational load-displacement, load-crack extension, crack extension-displacement and J-R curves agree reasonably well with the experimental data. However, the computational displacement corresponding to the computational maximum load of the computational load-displacement curve is smaller than the corresponding experimental value as shown in Figure 8(a). As shown in Figure 8(b), the computational crack extension of the computational load-crack extension curve at the computational maximum load is smaller than the corresponding experimental value. Also, as shown in Figure 8(b), the computational load and slope of the computational load-crack extension curve for the crack extension larger than that corresponding to the computational maximum load are different from those of the experimental data. As shown in Figure 8(c), the crack extension of the computational crack extension-displacement curve is smaller than the experimental data for small displacements. As the displacement increases, the computational crack extension is larger than the corresponding experimental value. The computational J-R curve is obtained based on the computational load, displacement, and crack extension by following the procedure to determine the experimental J-R curves as presented in Kim et al. [21] based on the results of their three-dimensional finite element analyses. Kim et al. [21] suggested that the J integral for the A(T) specimens can be calculated as the sum of the elastic component obtained by the equations for A(T) specimens in the ASTM Standard E399 [30] and the plastic

component obtained by the equations for compact tension specimens in the ASTM Standard E1820 [31]. As shown in Figure 8(d), the computational J integral is larger than the experimental J integral for small crack extensions. As the crack extension increases, the computational J integral becomes less than and then larger than the experimental data.

The computational load-displacement, load-crack extension, crack extension-displacement and J-R curves with the fixed cohesive parameters for the hydrogen-charged H94-54 specimen are compared with the experimental data in Figures 9(a), 9(b), 9(c), and 9(d), respectively. Similar differences as those discussed for Figures 8(a) to 8(d) for the uncharged H94-2 specimen are still observed in the computational load-displacement, load-crack extension, crack extension-displacement and J-R curves for the hydrogen-charged H94-54 specimen as shown in Figures 9(a) to 9(d). But with the smaller differences as shown in Figures 9(a) to 9(d), the computational load-displacement, load-crack extension, crack extension-displacement and J-R curves can be stated to agree well with the experimental data for the hydrogen-charged H94-54 specimen when the small differences are ignored. For the uncharged H94-2 specimen, the differences of the computational and experimental load-crack extension, crack extension-displacement and J-R curves as shown in Figures 8(b) to 8(d) are much larger than those for the hydrogen-charged H94-54 specimen as shown in Figures 9(b) to 9(d). The large differences should not be ignored and should be investigated further.

5. Computational Results Based on Varying Cohesive Parameters

The results of the finite element analyses with the fixed cohesive parameters were shown to have reasonable computational load-displacement curves when compared with the experimental data for uncharged and tritium-charged-and-decayed A(T) specimens in Wu et al.

[6]. However, the computational load-crack extension and crack extension-displacement curves showed some differences from the experimental data for uncharged and tritium-charged-and-decayed A(T) specimens in Wu et al. [6]. Similarly, the computational load-crack extension and crack extension-displacement curves for the hydrogen-charged H94-54 specimen showed some differences from the experimental data in this investigation. In order to improve the computational load-crack extension and crack extension-displacement curves for uncharged and hydrogen-charged A(T) specimens, finite element analyses with varying cohesive parameters are conducted by considering the cohesive parameters as functions of the crack extension. The procedures to select the varying cohesive parameters are detailed in Appendix A.

Tables 5 and 6 list the selected sets of the cohesive strength T_0, the cohesive energy Γ_0, and the softening ratio δ_2/δ_0 for the cohesive elements with different radial distances to the initial crack tips for the uncharged H94-2 and hydrogen-charged H94-54 A(T) specimens, respectively. For the selected sets, the cohesive parameters are kept constants for a few neighboring cohesive elements. Figures 10(a) and 10(b) show the cohesive strength function and cohesive energy function of the radial distance to the initial crack tip compared with the reference fixed cohesive strength and fixed cohesive energy for the uncharged H94-2 specimen, respectively. As shown in Figure 10(a), the cohesive strength for the uncharged H94-2 specimen increases from the initial crack tip to the crack extension of 0.3 mm, decreases from the crack extension of 0.5 mm, and remains as a constant as the crack extension increases. As shown in Figure 10(b), the cohesive energy for the uncharged H94-2 specimen increases from the initial crack tip to the crack extension of 0.7 mm, decreases and remains as a constant as the crack extension increases. It should be noted that the general trend of the cohesive energy for the uncharged H94-2 specimen is based on the general trend of the separation work rate in the same

specimen with the nodal release method to simulate the crack extension as presented in Sung et al. [22]. Similarly, Figures 11(a) and 11(b) show the cohesive strength function and cohesive energy function of the radial distance to the initial crack tip compared with the reference fixed cohesive strength and fixed cohesive energy for the hydrogen-charged H94-54 specimen, respectively. As shown in Figure 11(a), the cohesive strength increases from the initial crack tip to the crack extension of 0.4 mm, decreases from the crack extension of 0.4 mm, and remains as a constant as the crack extension increases. As shown in Figure 11(b), the cohesive energy for the hydrogen-charged H94-54 specimen increases from the initial crack tip to the crack extension of 0.6 mm and then decreases as the crack extension increases. It should be noted that the general trend of the cohesive energy for the hydrogen-charged H94-54 specimen is also based on the general trend of the separation work rate in the same specimen with the nodal release method to simulate the crack extension as presented in Sung et al [22].

As discussed earlier and in Appendix A, the cohesive strength and cohesive energy can be selected as functions of the crack extension to improve the computational load-crack extension and crack extension-displacement curves of A(T) specimens. The computational load-displacement, load-crack extension, crack extension-displacement and J-R curves with the varying cohesive parameters for the uncharged H94-2 specimen are compared with the experimental data in Figures 12(a), 12(b), 12(c) and 12(d), respectively. As shown in Figures 12(a) to 12(d), the computational load-displacement, load-crack extension, crack extension-displacement and J-R curves agree very well with the experimental data. The computational displacement and crack extension corresponding to the computational maximum load are compared well with the experimental data. Also, the computational load and slope of the computational load-crack extension curve for the entire range of the crack extensions are

compared well with the experimental data as shown in Figure 12(b). The computational crack extensions of the computational crack extension-displacement curve are in agreement with the experimental data as shown in Figure 12(c). The computational J-R curve is in good agreement with the experimental data as shown in Figure 12(d).

Since the experimental data of two more uncharged H94-1 and H94-4 specimens with different initial crack lengths are available, the selected varying cohesive parameters for the uncharged H94-2 specimen are then used for the finite element analyses of the uncharged H94-1 and H94-4 specimens. The computational results for the uncharged H94-1 and H94-4 specimens also agree well with the experimental data as shown in Appendix B.

The computational load-displacement, load-crack extension, crack extension-displacement and J-R curves with the varying cohesive parameters for the hydrogen-charged H94-54 specimen are compared with the experimental data in Figures 13(a), 13(b), 13(c) and 13(d), respectively. As shown in Figures 13(a) to 13(d), the computational load-displacement, load-crack extension, crack extension-displacement and J-R curves agree very well with the experimental data. The computational displacement and crack extension corresponding to the computational maximum load are compared well with the experimental data. Also, the computational load and slope of the computational load-crack extension curve for the entire range of the crack extensions are compared well with the experimental data as shown in Figure 13(b). The computational crack extensions of the computational crack extension-displacement curve are in good agreement with the experimental data as shown in Figure 13(c). The computational J-R curve is in good agreement with the experimental data as shown in Figure 13(d).

Figure 16(a) shows the computational load-displacement curves for different element sizes of 0.025 mm, 0.05 mm and 0.1 mm near the crack tip based on the same identified varying cohesive parameters as shown in Figure 10 and in Table 5 for comparison with the experimental load-displacement curve for the uncharged H94-2 specimen. Figure 16(b) shows the computational total work, elastic strain energy, plastic dissipation and cohesive energy as functions of the displacement for different element sizes of 0.025 mm, 0.05 mm and 0.1 mm for the uncharged H94-2 specimen. The computational total work is the sum of the computational elastic strain energy, plastic dissipation and cohesive energy. As shown in Figure 16(a), the computational load-displacement curve is slightly lower with a larger element size which results in a lower computational plastic dissipation outside of the cohesive zone and a lower computational total work as shown in Figure 16(b). Overall, the computational results are similar for the given different element sizes, scaled with the crack tip opening displacement, as shown in Figures 16(a) and 16(b).

6. Discussions

6.1 Comparisons of Fixed and Varying Cohesive Parameters Approaches

The computational load-displacement, load-crack extension, crack extension-displacement and J-R curves with the fixed and varying cohesive parameters for the uncharged H94-2 specimen are compared with the experimental data in Figures 14(a), 14(b), 14(c) and 14(d), respectively. As shown in Figure 14, the computational results with the fixed cohesive parameters can fit the experimental load-displacement curve well while the computational load-crack extension and crack extension-displacement curves show some differences from the experimental data. The computational load-crack extension and crack extension-displacement

curves with the varying cohesive parameters can fit the experimental data well. The computational results indicate that the computational displacement and crack extension corresponding to the maximum load can be adjusted to fit the experimental data with the varying cohesive parameters.

The average cohesive strength $\overline{T}_0$ and the average cohesive energy $\overline{\Gamma}_0$ are defined as

$$\overline{T}_0 = \frac{\int T_0 \mathrm{d}(\Delta a)}{\Delta a_f} \tag{2}$$

and

$$\overline{\Gamma}_0 = \frac{\int \Gamma_0 \mathrm{d}(\Delta a)}{\Delta a_f} \tag{3}$$

Here, Δa represents the crack extension and Δa_f represents the final crack extension measured from the experiment. The values of the average cohesive strength $\overline{T}_0$ and cohesive energy $\overline{\Gamma}_0$ of the varying cohesive parameters and the values of the fixed cohesive strength T_0 and cohesive energy Γ_0 for the uncharged H94-2 and the hydrogen-charged H94-54 specimens are listed in Table 7. As listed in Table 7, the average cohesive strength $\overline{T}_0$ and cohesive energy $\overline{\Gamma}_0$ of the varying cohesive parameters are close to the fixed cohesive strength T_0 and cohesive energy Γ_0, respectively. This suggests that the computational load-displacement curve depends on the fixed cohesive strength and energy or the average cohesive strength and energy. Since the selected fixed cohesive parameters and average varying cohesive parameters are close, the computational load-displacement curves with the fixed and varying cohesive parameters are close and both can fit the experimental load-displacement curve well. But the computational load-crack extension

and crack extension-displacement curves with the fixed cohesive parameters have some differences from the experimental data.

The varying cohesive parameters can be used to improve the computational load-crack extension and crack extension-displacement curves by considering the cohesive parameters as functions of the crack extension in the phenomenological way. This suggests that the computational load-crack extension and crack extension-displacement curves depend on the variations of the cohesive parameters at different crack extensions. Therefore, the CZM approach with the fixed cohesive parameters cannot be used to fit the experimental load-crack extension and crack extension-displacement curves well because the variations of the cohesive parameters as functions of the crack extension are not considered.

Similar comparisons of the computational results with the fixed and varying cohesive parameters can be shown in Figures 15(a), 15(b), 15(c) and 15(d) for the hydrogen-charged H94-54 specimen. It should be noted that the varying cohesive parameters for the hydrogen-charged H94-54 specimen as shown in Figures 11(a) and 11(b) have smaller variations when compared with those for the uncharged H94-2 specimen as shown in Figures 10(a) and 10(b). As shown in Figures 14(b), 14(c), 15(b), and 15(c), the differences of the computational load-crack extension and crack extension-displacement curves of the hydrogen-charged H94-54 specimen are smaller than those of the uncharged H94-2 specimen. Therefore, only small variations of the cohesive parameters are needed to improve the computational load-crack extension and crack extension-displacement curves for the hydrogen-charged H94-54 specimen.

6.2 Experimental J-R Curves of A(T) Specimens

The fixed cohesive parameters of the fixed cohesive parameter approach are used as the reference cohesive parameters to start the iteration process for the varying cohesive parameters of the varying cohesive parameter approach. For the fixed cohesive parameter approach, the experimental J integrals at the deviation loads are very important to determine the reference cohesive energies to start the iteration process to select the cohesive energies for the fixed cohesive parameter approach. Table 8 lists the maximum opening stresses determined from the finite element analyses without cohesive elements, the selected fixed cohesive strengths, the experimental J integrals at the deviation loads, the selected fixed cohesive energies, the experimental J integrals at the maximum loads, and the values of $J_{0.2}$ determined from the blunting lines based on the ASTM Standard E1820 [31] for the uncharged H94-2 and hydrogen-charged H94-54 specimens. As listed in Table 8, the selected fixed cohesive strengths of 2,650 MPa and 2,850 MPa are close to the maximum opening stresses of 2,619 MPa and 2,818 MPa for the uncharged H94-2 and hydrogen-charged H94-54 specimens, respectively. Also, the selected cohesive energies of 35 kJ/m^2 and 22 kJ/m^2 are close to the experimental J integrals of 30.1 kJ/m^2 and 23.6 kJ/m^2 at the deviation loads for the uncharged H94-2 and hydrogen-charged H94-54 specimens, respectively. However, the experimental J integrals at the maximum loads and the values of $J_{0.2}$ from the blunting lines based on the ASTM Standard E1820 [31] are much larger than the selected cohesive energies for the uncharged H94-2 and hydrogen-charged H94-54 specimens. Therefore, the experimental J integrals at the deviation loads should be selected as the reference cohesive energies to start the iteration process to select the fixed cohesive energies for the small uncharged H94-2 and hydrogen-charged H94-54 specimens.

6.3 Separation Work Rate, Maximum Opening Stress and Plastic Zone Size and Shape

Sung et al. [22] conducted two-dimensional plane strain finite element analyses with the nodal release method by following the experimental crack extension-displacement curves for the uncharged H94-2 and hydrogen-charged H94-54 A(T) specimens of CF stainless steels. The nodal release method was adopted to calculate the negative work per unit crack area as the separation work rate for an increment of the crack area for a given increment of the displacement. The detailed procedures of the nodal release method were reported in Sung et al. [22]. Sung et al [22] obtained the separation work rates and the maximum opening stresses ahead of the crack tips as functions of the crack extension for the uncharged H94-2 and hydrogen-charged H94-54 A(T) specimens. The results of the separation work rate and the maximum opening stress ahead of the crack tip for the uncharged H94-2 specimen are presented in Figures 17(a) and 17(b), respectively. The selected varying cohesive energy and varying cohesive strength for the A(T) specimen are also shown in Figures 17(a) and 17(b), respectively, for comparison. The general trend of the computational separation work rate is similar to the selected the cohesive energy for the uncharged H94-2 A(T) specimen as shown in Figure 17(a). The general trend of the computational maximum opening stress ahead of the crack tip is similar to the selected cohesive strength for the uncharged H94-2 A(T) specimen as shown in Figure 17(b). The results for a comparison of the separation work rate and maximum opening stress ahead of the crack tip with the selected varying cohesive energy and varying cohesive strength for the hydrogen-charged H94-54 A(T) specimen are similar to those in Figures 17(a) and 17(b) and therefore are not shown here. The general trends of the computational separation work rates obtained with the nodal release method are the motivation for the selected varying cohesive energy functions for these small A(T) specimens.

Sung et al. [22] also examined the maximum values of the stress triaxiality ahead of the growing crack tips with the nodal release method. Note that the stress triaxiality is defined as the ratio of the mean stress to the von Mises equivalent stress. The computational results of Sung et al. [22] indicated that the maximum values of the stress triaxiality ahead of the growing crack tips are relatively constant with the values from 2.30 to 2.54 and from 2.47 to 2.51 for the uncharged H94-2 and hydrogen-charged H94-54 A(T) specimens, respectively. The relatively constant maximum values of the stress triaxiality ahead of the growing crack tips indicate the stress triaxiality may not be a major factor for the selected varying cohesive parameters.

Kim et al. [21] conducted three-dimensional finite element analyses of a side-grooved A(T) specimen of CF 21-6-9 stainless steel. Their computational results indicated that the crack tip fields along the crack front are near plane strain conditions with a higher plane strain constraint parameter at the center plane of the specimen and a lower plane strain constraint parameter near the free surfaces of the specimen. The side grooves in the A(T) specimens promote the flat fracture but the crack tip fields along the crack front are not completely under plane strain conditions. Therefore, the A(T) specimens can be considered as small thin specimens. As for the small thin CCT specimen as discussed earlier, the increase part of the cohesive energy can be due to the increase of the free surface effect because of the decrease of the plane strain portion of the crack front from the increase of the plastic zone size along the crack front when the crack extension increases. The separation work rate as shown in Figure 17(a) catches the trend of the increasing cohesive energy from the energy viewpoint. It should be mentioned that the initial stage of the crack extension is highly three-dimensional in the A(T) specimens. The crack extension in the A(T) specimen should be modeled by a full three-dimensional finite element analysis to catch the evolution of the constraint conditions along the

crack front as the crack extension increases. However, the two-dimensional plane strain finite element analysis with the nodal release method can also catch the general trend of the increasing separation work rate for selection of the varying cohesive energy as shown in Figure 17(a). The decrease part of the cohesive energy may be related to the changes of the plastic zone pattern and size in the small A(T) specimen. The plastic zone sizes and shapes in the uncharged H94-2 specimen at the deviation load of 1,385 N (crack initiation), at the maximum load of 2,070 N (crack extension of 0.25 mm), and at a large crack extension of 1.00 mm are shown in Figures 18(a), 18(b), and 18(c), respectively. As shown in Figure 18, as the crack extension increases, the plastic zone near the crack tip grows and the compressive plastic zone develops at the other side of the specimen. From the crack initiation to the crack extension corresponding to the maximum load, both the plastic zone near the tip and compressive plastic zone increase and connect together. After the connection of the plastic zones, the connected plastic zone is limited to the remaining ligament. As the crack extension increases further, the plastic zone size decreases. The decrease of the plastic zone size may be the reason resulting in the slight decrease of the cohesive energy when the crack extension further increases to reach to the final crack length.

7. Conclusions

Two-dimensional plane strain finite element analyses with the cohesive zone modeling approach are adopted to model crack extensions in uncharged and hydrogen-charged arc-shaped tension A(T) specimens of conventionally forged 21-6-9 austenitic stainless steels. Finite element analyses with fixed cohesive parameters are conducted first to select the cohesive parameters to fit the maximum loads of the experimental load-displacement curves for uncharged

and hydrogen-charged A(T) specimens. The experimental J integrals at the deviation loads determined from the finite element analyses of the A(T) specimens without cohesive elements are taken as the reference cohesive energies and the maximum opening stresses ahead of the initial crack tips determined from the finite element analyses of the A(T) specimens without cohesive elements are taken as the reference cohesive strengths to calibrate cohesive parameters. The computational load-displacement curves for uncharged and hydrogen-charged A(T) specimens from the finite element analyses with the calibrated fixed cohesive parameters can fit well the experimental data.

Finite element analyses with varying cohesive parameters are then conducted to improve the computational load-crack extension and crack extension-displacement curves for uncharged and hydrogen-charged A(T) specimens. The cohesive energies are assumed to be functions of the crack extension in the phenomenological way with the initial values smaller than the experimental J integrals at the deviation loads, increase and then decrease as the crack extension increases for uncharged and hydrogen-charged A(T) specimens. The cohesive strengths are also selected as functions of the crack extension similar to those of the cohesive energies to fit the experimental load-crack extension curves. The computational load-crack extension and crack extension-displacement curves agree quiet well with the experimental data for uncharged and hydrogen-charged A(T) specimens with the selected varying cohesive parameters. The cohesive energies and the cohesive strengths as functions of the crack extension appear to follow the general trends of the separation work rates and the maximum opening stresses ahead of the crack tips in the two-dimensional plane strain finite element analyses with the nodal release method to simulate crack extensions in uncharged and hydrogen-charged A(T) specimens. The lower selected cohesive energy and higher selected cohesive strength for the hydrogen-charged A(T)

specimen indicate the effects of hydrogen on the fracture properties of A(T) specimens of 21-6-9 austenitic stainless steels.

Finally, for a thin structure or a small thin fracture specimen, the plane strain conditions may not be satisfied along the majority of the crack front at crack initiation and during the initial crack extension less than the structure or specimen thickness. The computational results presented in this paper indicate that for modeling of crack extension in a thin structure or a small thin specimen, the cohesive energy and cohesive strength can vary as functions of the crack extension when the majority of the crack front does not satisfy the plane strain conditions at crack initiation and during crack extension.

Acknowledgement

The support of this research by the U.S. Department of Energy is appreciated. Helpful discussions with Dr. Shin-Jang Sung of University of Michigan are appreciated.

References

[1] Roychowdhury S, Arun Roy YD, Dodds RH. Ductile tearing in thin aluminum panels: Experiments and analyses using large-displacement, 3-D surface cohesive elements. Eng Fract Mech 2002;69:983–1002. https://doi.org/10.1016/S0013-7944(01)00113-8.

[2] Cornec A, Scheider I, Schwalbe KH. On the practical application of the cohesive model. Eng Fract Mech 2003;70:1963–87. https://doi.org/10.1016/S0013-7944(03)00134-6.

[3] Scheider I, Brocks W. Simulation of cup-cone fracture using the cohesive model. Eng Fract Mech 2003;70:1943–61. https://doi.org/10.1016/S0013-7944(03)00133-4.

[4] Scheider I, Brocks W. Cohesive elements for thin-walled structures. Comput Mater Sci 2006;37:101–9. https://doi.org/10.1016/j.commatsci.2005.12.042.

[5] Sung S-J, Pan J, Korinko PS, Morgan M, McWillliams A. Simulations of fracture tests of uncharged and hydrogen-charged additively manufactured 304 stainless steel specimens using

cohesive zone modeling. Eng Fract Mech 2019;209:125–46. https://doi.org/10.1016/j.engfracmech.2019.01.006.

[6] Wu S, Pan J, Korinko PS, Morgan M. Simulations of crack extensions in arc-shaped tension specimens of uncharged and tritium-charged-and-decayed 21-6-9 austenitic stainless steels using cohesive zone modeling. Am Soc Mech Eng Press Vessel Pip Div PVP 2020;PVP 2020-43542.

[7] Schwalbe KH, Scheider I, Cornec A. Guidelines for applying cohesive models to the damage behaviour of engineering materials and structures. Springer Berlin Heidelberg 2013.

[8] Simonsen BC, Törnqvist R. Experimental and numerical modelling of ductile crack propagation in large-scale shell structures. Mar Struct 2004;17:1–27. https://doi.org/10.1016/j.marstruc.2004.03.004.

[9] Woelke PB, Shields MD, Hutchinson JW. Cohesive zone modeling and calibration for mode I tearing of large ductile plates. Eng Fract Mech 2015;147:293–305. https://doi.org/10.1016/j.engfracmech.2015.03.015.

[10] Nielsen KL, Hutchinson JW. Cohesive traction-separation laws for tearing of ductile metal plates. Int J Impact Eng 2012;48:15–23. https://doi.org/10.1016/j.ijimpeng.2011.02.009.

[11] Andersen RG, Felter CL, Nielsen KL. Micro-mechanics based cohesive zone modeling of full scale ductile plate tearing: From initiation to steady-state. Int J Solids Struct 2019;160:265–75. https://doi.org/10.1016/j.ijsolstr.2018.10.027.

[12] Gurson AL. Continuum theory of ductile rupture by void nucleation and growth - 1. yield criteria and flow rules for porous ductile media. Am Soc Mech Eng 1976.

[13] Tvergaard V. Influence of voids on shear band instabilities under plane strain conditions. Int J Fract 1981;17:389–407. https://doi.org/10.1007/BF00036191.

[14] Tvergaard V, Needleman A. Analysis of the cup-cone fracture in a round tensile bar. Acta Metall 1984;32:157–69. https://doi.org/10.1016/0001-6160(84)90213-X.

[15] Sung S-J, Pan J, St Lawrence S, Scarth DA. Two-dimensional cohesive zone modeling of crack extensions in curved compact tension specimens of as-received and hydrided irradiated Zr-2.5Nb pressure tube materials. Accepted for publication in Engineering Fracture Mechanics, 2020, pending sponsor approval for publication.

[16] Sung S-J, Pan J, St Lawrence S, Scarth DA. Effects of curvature on ductile fracture initiation in curved compact tension specimens of hydrided irradiated Zr-2.5Nb materials with split circumferential hydrides. Eng Fract Mech 2019;211:180–97. https://doi.org/10.1016/j.engfracmech.2019.02.019.

[17] Sung S-J, Pan J, Lam PS, Scarth DA. Ductile fracture initiation with consideration of strain concentration and stress triaxiality near crack fronts in compact tension specimens of hydrided

irradiated Zr-2.5Nb materials with split circumferential hydrides. Eng Fract Mech 2017;186:208–41. https://doi.org/10.1016/j.engfracmech.2017.10.012.

[18] Sung S-J, Wu S, Pan J. Separation work rate for crack extension in a thin compact tension specimen with finite step nodal release method. Am Soc Mech Eng Press Vessel Pip Div PVP 2021;PVP 2021-62656.

[19] Siegmund T, Brocks W. The role of cohesive strength and separation energy for modeling of ductile fracture. ASTM Spec Tech Publ 1999:139–51.

[20] Siegmund T, Brocks W. A numerical study on the correlation between the work of separation and the dissipation rate in ductile fracture. Eng Fract Mech 2000;67:139–54. https://doi.org/10.1016/S0013-7944(00)00054-0.

[21] Kim Y, Chao YJ, Pechersky MJ, Morgan M. C-specimen fracture toughness testing: Effect of side grooves and η factor. J Press Vessel Technol Trans ASME 2004;126:293–9. https://doi.org/10.1115/1.1762425.

[22] Sung S-J, Pan J, Korinko PS, Morgan M. Simulations of fracture tests of arc-shaped tension specimens of austenitic stainless steels with consideration of hydrogen content using cohesive zone modeling. Research to be submitted for publication.

[23] Morgan M. Tritium aging effects on the fracture toughness properties of forged stainless steel. In: Wicks GG, Simon J, editors. Materials innovations in an emerging hydrogen economy; 2008, p. 223–235. https://doi.org/10.1002/9780470483428.ch23.

[24] Wu S, Sung S-J, Pan J, Lam P-S, Morgan M, Korinko PS. Modeling of crack extensions in arc-shaped specimens of hydrogen-charged austenitic stainless steels using cohesive zone model. Am Soc Mech Eng Press Vessel Pip Div PVP 2018;6A-2018:1–8. https://doi.org/10.1115/PVP2018-84919.

[25] Morgan M. The effects of hydrogen isotopes and helium on the flow and fracture properties of 21-6-9 stainless steel. In: Liaw PK, Weertman JR, Marcus HL, Santner JS, editors. Morris E. Fine Symposium, 1991, p. 105–111.

[26] Park K, Paulino GH, Roesler JR. A unified potential-based cohesive model of mixed-mode fracture. J Mech Phys Solids 2009;57:891–908. https://doi.org/10.1016/j.jmps.2008.10.003.

[27] Park K, Paulino GH. Computational implementation of the PPR potential-based cohesive model in ABAQUS: Educational perspective. Eng Fract Mech 2012;93:239–62. https://doi.org/10.1016/j.engfracmech.2012.02.007.

[28] Borchers C, Michler T, Pundt A. Effect of hydrogen on the mechanical properties of stainless steels. Adv Eng Mater 2008;10:11–23. https://doi:10.1002/adem.200700252.

[29] Jemblie L, Olden V, Akselsen OM. A review of cohesive zone modelling as an approach for numerically assessing hydrogen embrittlement of steel structures. Philos Trans R Soc A Math Phys Eng Sci 2017;375:1-15. https://doi:10.1098/rsta.2016.0411.

[30] ASTM Standard E399. Standard Test Method for Plane-Strain Fracture Toughness of Metallic Materials 1. ASTM B Stand 1997;90:1–31. https://doi.org/10.1520/E0399-19.

[31] ASTM Standard E1820. Standard Test Method for Measurement of Fracture Toughness. ASTM B Stand 2013:1–54. https://doi.org/10.1520/E1820-18.

Appendix A. Selection Processes of Varying Cohesive Parameters

The computational load-displacement curves for the uncharged H94-2 and hydrogen-charged H94-54 specimens with the fixed cohesive parameters can fit well the experimental load-displacement curves. The computational load-crack extension, crack extension-displacement and J-R curves can fit the experimental data but show some differences from the experimental curves as discussed in the main text. In order to fit well the experimental load-crack extension and crack extension-displacement data for the uncharged H94-2 and hydrogen-charged H94-54 specimens, finite element analyses with different sets of varying cohesive parameters are conducted. The processes to select the varying cohesive parameters are divided into two steps. The first step is to select the varying cohesive parameters to fit the experimental load-crack extension curve from the crack initiation to the maximum load. The second step is to select the varying cohesive parameters to fit the experimental load-crack extension curve for the crack extension larger than that corresponding to the maximum load. The experimental load-displacement curve is also used as the second reference to select the varying cohesive parameters in the two steps. It should be mentioned again that the smooth trapezoidal traction-separation law should be used with a very small initial δ_1/δ_0 ratio to fit the initial near linear elastic response of the load-displacement curve.

The selection processes for the two steps for the uncharged H94-2 specimen are discussed first. For the first step, five cases of A, B, C, D, and E, with the varying cohesive parameters are considered. Figures A1(a) and A1(b) show the cohesive strength and cohesive energy functions, respectively, for Cases A, B, and C. Figure A1(a) shows that Case A has the fixed cohesive strength of 2,750 MPa for the entire range of the radial distance ahead of the initial crack tip. Cases B and C have the lower cohesive strengths of 2,375 MPa and 2,000 MPa,

respectively, for the radial distance ahead of the initial crack tip from 0 mm to 0.25 mm. Cases B and C have the higher cohesive strength of 2,750 MPa for the radial distance ahead of the initial crack tip larger than 0.25 mm. It should be noted that 0.25 mm is the experimental crack extension corresponding to the experimental maximum load of the uncharged H94-2 specimen and also of the uncharged H94-1 and H94-4 specimens. Cases A, B, and C have the same lower cohesive energy of 20 kJ/m^2 for the radial distance ahead of the initial crack tip from 0 mm to 0.25 mm and the same higher cohesive energy of 40 kJ/m^2 for the radial distance ahead of the initial crack tip larger than 0.25 mm. The selections are motivated by the small computational crack extension for the initial stage of crack extension from the finite element analysis for the uncharged H94-2 specimen with the fixed cohesive parameters.

Figure A2(a) shows a comparison of the computational load-displacement curves for Cases A, B, and C with the experimental load-displacement curve. The computational load-displacement curves of Cases A and B with the higher cohesive strengths near the initial crack tip are higher than the experimental load-displacement curve near the displacement of 0.2 mm. The reason is that the first few cohesive elements near the initial crack tip in Cases A and B can only open up at the higher loads because of the selected higher cohesive strengths ahead of the initial crack tip. The computational results for Case C give a slightly lower load-displacement curve and the computational results can fit the general trend of the experimental load-displacement curve for the small displacements because of the lower cohesive strength of 2,000 MPa selected ahead of the initial crack tip. Figure A2(b) shows a comparison of the computational load-crack extension curves for Cases A, B, and C with the experimental load-crack extension curve. As shown in Figure A2(b), Cases A, B, and C give large amounts of crack extensions at the loads near 1,500 N. The computational results for Cases B and C have

the lower load-crack extension curves because of their lower cohesive strengths for the radial distance ahead of the initial crack tip from 0 mm to 0.25 mm while Case A has a slightly higher load-crack extension curve when compared with the experimental load-crack extension curve because of the higher cohesive strength for the radial distance ahead of the initial crack tip from 0 mm to 0.25 mm. The results indicate that the varying cohesive parameters to fit the experimental load-crack extension curve from the crack initiation to the maximum load could be in the range of the cohesive parameters selected for Case A and Case C.

Figures A3(a) and A3(b) show the cohesive strength and cohesive energy functions, respectively, for Cases C, D, and E. Figure A3(a) shows that Cases C, D, and E have the same lower cohesive strength of 2,000 MPa and cohesive energy of 20 kJ/m^2 ahead of the initial crack tip, and the same higher cohesive strength of 2,750 MPa and cohesive energy of 40 kJ/m^2 away from the initial crack tip. Cases D, E, and C have the increases of the cohesive strength and cohesive energy at the radial distance ahead of the initial crack tip at 0.075 mm, 0.15 mm, and 0.25 mm, respectively.

Figure A4(a) shows a comparison of the computational load-displacement curves for Cases C, D, and E with the experimental load-displacement curve. The computational load-displacement curves of Cases D and E with the increases of the cohesive strength and cohesive energy at the smaller radial distances ahead of the initial crack tip are higher than the experimental load-displacement curve near the displacement of 0.2 mm although they have the same low cohesive strength and cohesive energy as those selected for Case C ahead of the initial crack tip. Figure A4(b) shows a comparison of the computational load-crack extension curves for Cases C, D, and E with the experimental load-crack extension curve. In Figure A4(b), the maximum loads for Cases D and E are reached at the smaller crack extensions because of their

increases of the cohesive strengths and the cohesive energies at the smaller radial distances ahead of the initial crack tip. The computational maximum load for Case C is reached at the computational crack extension of 0.25 mm which agrees with that of the experimental load-crack extension curve. However, the computational load-crack extension curve is lower than the experimental load-crack extension curve. The results indicate that the varying cohesive parameters to fit the experimental load-crack extension curve from the crack initiation to the maximum load could be an increasing function of the radial distance ahead of the initial crack tip in the range of 0 mm to 0.25 mm such that the computational crack extension corresponding to the maximum load could fit the experimental data.

More finite element analyses were conducted to select the varying cohesive parameters to fit the computational load-crack extension curve to the experimental load-crack extension curve from the crack initiation to the maximum load with the cohesive strength selected in the range of 2,000 MPa to 2,750 MPa and cohesive energy selected in the range of 20 kJ/m^2 to 40 kJ/m^2 for the radial distance ahead of the initial crack tip from 0 mm to 0.25 mm. The selected cohesive strength and cohesive energy functions for Case 1 are shown as the blue lines in Figures A5(a) and A5(b), respectively. The computational load-displacement, load-crack extension, and crack extension-displacement curves for Case 1 are shown as the blue dashed lines in Figures A6(a), A6(b), and A6(c), respectively. As shown in Figures A6(a), A6(b) and A6(c), the computational displacement and crack extension corresponding to the experimental maximum load are in agreement with the experimental data. However, the computational load and slope of the computational load-crack extension curve for the crack extension larger than that corresponding to the experimental maximum load are still different from those of the experimental data. Therefore, the cohesive strength and cohesive energy functions shown as the blue lines in

Figures A5(a) and A5(b) should be extended to a larger radial distance ahead of the initial crack tip instead of the crack extension corresponding to the experimental maximum load.

For the second step, Case 1 described above is used as the reference case and the cohesive strength and cohesive energy continue to be functions of the radial distance ahead of the initial crack tip to fit the load and slope of the experimental load-crack extension curve for the crack extension larger than that corresponding to the experimental maximum load. Based on the computational results from several finite element analyses, the general effects of the cohesive strength, cohesive energy and softening ratio on the load-displacement curve are shown in Figure A6(a). Under the conditions of the same cohesive energy and softening ratio, a lower cohesive strength will result in less plastic dissipation outside the cohesive zone. Therefore, the load-displacement curve moves to the left and down. Under the conditions of the same cohesive strength and softening ratio, a lower cohesive energy will result in less cohesive energy inside the cohesive zone, and consequently, less total external work with the same plastic dissipation due to the same cohesive strength. Therefore, the load-displacement curve moves to the left and down. Under the conditions of the same cohesive strength and cohesive energy, a lower softening ratio will result in larger final separation in the cohesive zone and less plastic dissipation outside the cohesive zone. Therefore, the load-displacement curve moves to the left and down. These trends are schematically shown in Figure A6(a).

As shown in Figure A6(b), under the conditions of the same cohesive energy and softening ratio, a decrease of the cohesive strength will lower the load-crack extension curve because the load required to extend the crack will be lower with a lower cohesive strength. Under the conditions of the same cohesive strength and softening ratio, an increase of the cohesive energy will move the load-crack extension curve to the left because the crack extension

at a given load is smaller with a higher cohesive energy. Figure A6(c) shows the effect of softening ratio δ_2/δ_0 on the crack extension-displacement curve. Under the conditions of the same cohesive strength and cohesive energy, an increase of the softening ratio will move the crack extension-displacement curve to the right. This is because the cohesive elements with a large softening ratio are stiffer such that the continuum elements near the cohesive zone will have more deformation which results in a larger crack mouth opening displacement.

In order to fit the experimental load-displacement and load-crack extension curve, the cohesive strength and cohesive energy functions have to be increasing functions to certain crack extensions and then become decreasing functions. It should be noted that in this paper, the varying cohesive energy follows the general trend of the separation work rate in the same A(T) specimen with the nodal release method to simulate the crack extension as shown in Sung et al. [19]. Several more finite element analyses were conducted to select the varying cohesive parameters in order to obtain the computational load-crack extension curve to fit the experimental load-crack extension curve for the crack extension larger than that corresponding to the maximum load. The best-fit case (Case 2) of the cohesive strength and cohesive energy functions for the uncharged H94-2 specimen are obtained and shown in Figures A5(a) and A5(b) or Figures 10(a) and 10(b), respectively. The computational load-displacement, load-crack extension, and crack extension-displacement curves for Case 2 are shown as red dashed lines in Figures A6(a), A6(b) and A6(c), respectively. As shown in the figures, the computational results agree very well with the experimental data.

Appendix B. Additional Computational Results for Uncharged H94-1 and H94-4 A(T) Specimens

The experimental load-displacement-crack extension data of two more uncharged A(T) H94-1 and H94-4 specimens with different initial crack lengths are available. The selected varying cohesive parameters for the uncharged H94-2 specimen with the initial crack length of 5.75 mm are then used for the finite element analyses of the uncharged H94-1 and H94-4 specimens with the smaller initial crack lengths of 5.37 mm and 4.95 mm, respectively. The values of the initial crack length a_0 and the initial COD's for the uncharged H94-1 and H94-4 A(T) specimens are listed in Table 1. As listed in Table 1, the initial crack lengths of the uncharged H94-1 and H94-4 specimens are smaller than that of the uncharged H94-2 specimen.

The computational load-displacement, load-crack extension, crack extension-displacement and J-R curves with the varying cohesive parameters for the uncharged H94-1 specimen are compared with the experimental data in Figures B1(a), B1(b), B1(c) and B1(d), respectively. As shown in Figures B1(a) to B1(d), the computational load-displacement, load-crack extension, crack extension-displacement and J-R curves agree well with the experimental data. The computational load-displacement, load-crack extension, crack extension-displacement and J-R curves with the varying cohesive parameters for the uncharged H94-4 specimen are compared with the experimental data in Figures B2(a), B2(b), B2(c) and B2(d), respectively. As shown in Figures B2(a) to B2(d), the computational load-displacement, load-crack extension, crack extension-displacement and J-R curves agree well with the experimental data.

Table 1. The dimensions of the initial crack length a_0, the thickness B, the net thickness B_n, and the initial crack mouth opening displacement (COD) for the uncharged and hydrogen-charged A(T) specimens.

	a_0 (mm)	B (mm)	B_n (mm)	COD (mm)
Uncharged H94-1 specimen	5.37	4.57	3.81	2.57
Uncharged H94-2 specimen	5.75	4.57	3.81	2.59
Uncharged H94-4 specimen	4.95	4.57	3.81	2.49
Hydrogen-charged H94-54 specimen	4.82	4.57	3.81	2.54

Table 2. The material constants for the uncharged and hydrogen-charged CF 21-6-9 steels.

	E (GPa)	ν	σ_Y (MPa)	K (MPa)	n
Uncharged steel	177.33	0.3	856.48	1,770	0.225
Hydrogen-charged steel	177.33	0.3	867.53	1,793	0.225

Table 3. The deviation loads, the J integrals at the deviation loads, and the maximum opening stresses for the uncharged H94-2 and hydrogen-charged H94-54 A(T) specimens.

	Deviation load (N)	J integral at deviation load (kJ/m^2)	Maximum opening stress (MPa)
Uncharged H94-2 specimen	1,385	30.1	2,619
Hydrogen-charged H94-54 specimen	2,717	23.6	2,814

Table 4. The fixed cohesive parameters for the smooth trapezoidal traction-separation law for the uncharged H94-2 and hydrogen-charged H94-54 A(T) specimens.

	T_0 (MPa)	Γ_0 (kJ/m^2)	δ_1/δ_0	δ_2/δ_0	δ_0 (μm)	δ_1 (μm)	δ_2 (μm)
Uncharged H94-2 specimen	2,650	35.0	0.005	0.6	16.55	0.082	9.9
Hydrogen-charged H94-54 specimen	2,850	22.0	0.005	0.5	10.35	0.052	5.2

Table 5. The varying cohesive parameters selected for the uncharged H94-2 A(T) specimen.

Radial distance to the initial crack tip (mm)	T_0 (MPa)	Γ_0 (kJ/m^2)	δ_2/δ_0
0-0.075	2,000	20	0.2
0.075-0.15	2,500	30	0.3
0.15-0.25	2,625	35	0.3
0.25-0.5	2,750	40	0.3
0.5-0.6	2,670	43	0.3
0.6-0.7	2,670	45	0.3
0.7-1.0	2,670	44	0.5
1.0-1.25	2,670	42	0.5
>1.25	2,670	40	0.5

Table 6. The varying cohesive parameters selected for the hydrogen-charged H94-54 A(T) specimen.

Radial distance to the initial crack tip (mm)	T_0 (MPa)	Γ_0 (kJ/m^2)	δ_2/δ_0
0-0.05	2,800	18	0.3
0.05-0.125	2,800	19	0.3
0.125-0.2	2,900	20	0.3
0.2-0.4	2,900	22	0.3
0.4-0.6	2,850	23	0.4
0.6-1.0	2,850	22	0.4
1.0-1.5	2,850	22	0.4
>1.5	2,850	21	0.4

Table 7. A comparison of the fixed cohesive parameters of the fixed cohesive parameter approach and the average cohesive parameters of the varying cohesive parameter approach for the uncharged H94-2 and hydrogen-charged H94-54 A(T) specimens.

	Approach	T_0 or $\overline{T}_0$ (MPa)	Γ_0 or $\overline{\Gamma}_0$ (kJ/m^2)
Uncharged H94-2 specimen	Fixed	2,650	35
	Varying (average)	2,646	39.88
Hydrogen-charged H94-54 specimen	Fixed	2,850	22
	Varying (average)	2,855	21.75

Table 8. The maximum opening stresses from the finite element analyses without cohesive elements, the selected fixed cohesive strengths, the experimental J integrals at the deviation loads, the selected fixed cohesive energies, the experimental J integrals at the maximum loads, and the values of $J_{0.2}$ from the blunting lines for the uncharged H94-2 and hydrogen-charged H94-54 A(T) specimens.

	Maximum opening stress (MPa)	Cohesive strength (MPa)	Exp J integral at deviation load (kJ/m^2)	Cohesive energy (kJ/m^2)	Exp J integral at maximum load (kJ/m^2)	$J_{0.2}$ from blunting line (kJ/m^2)
Uncharged H94-2 specimen	2,619	2,650	30.1	35.0	273	378
Hydrogen-charged H94-54 specimen	2,814	2,850	23.6	22.0	180	262

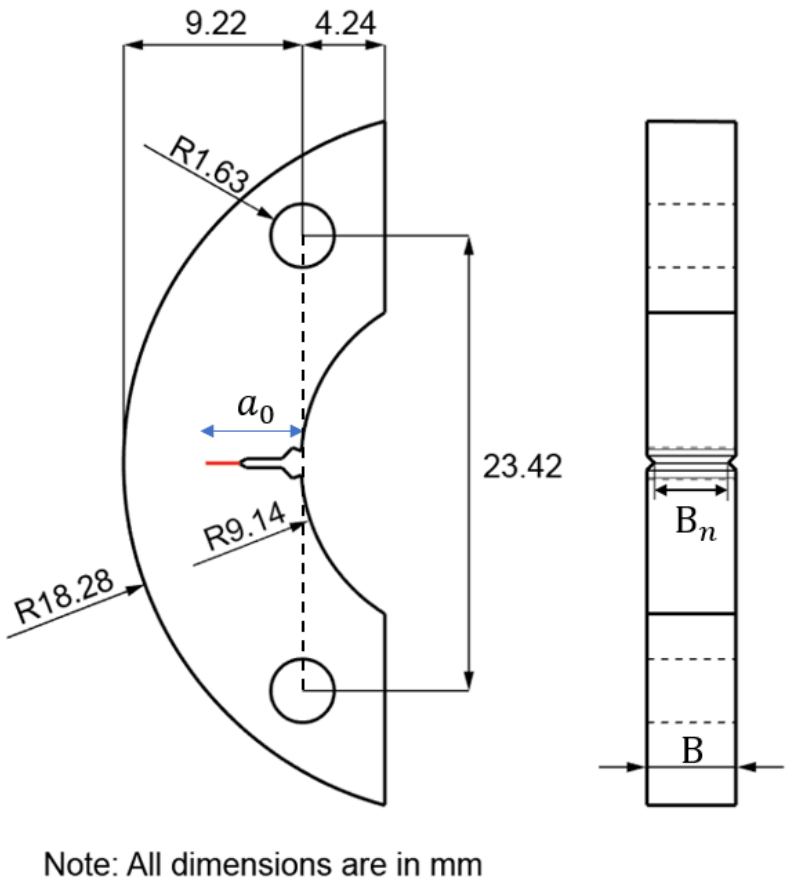

Figure 1. Schematics of side and front views of an A(T) specimen with side grooves.

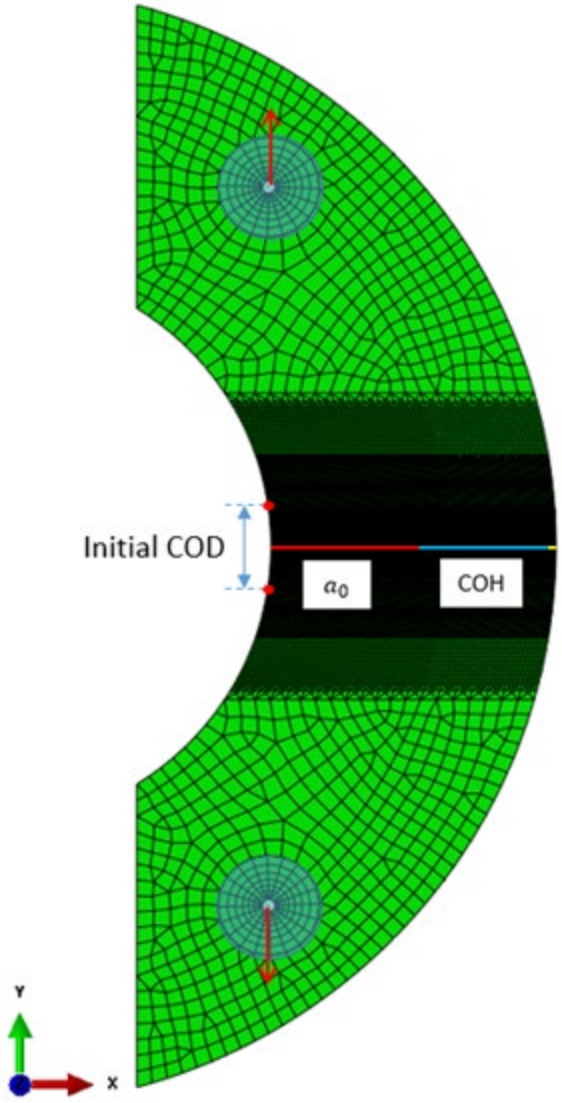

Figure 2. Finite element model for an A(T) specimen with cohesive elements.

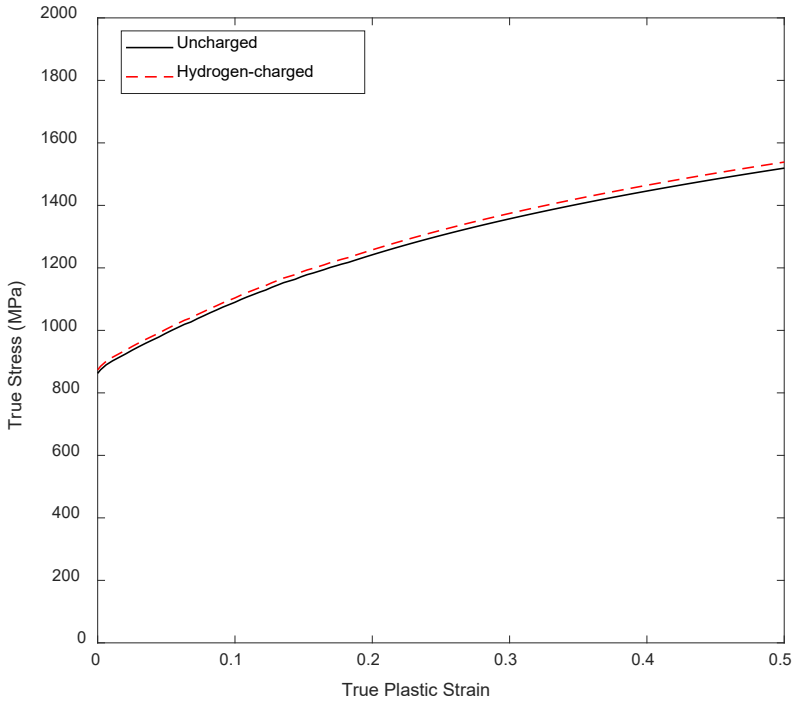

Figure 3. The true stress-plastic strain curves for the uncharged and hydrogen-charged CF 21-6-9 stainless steels.

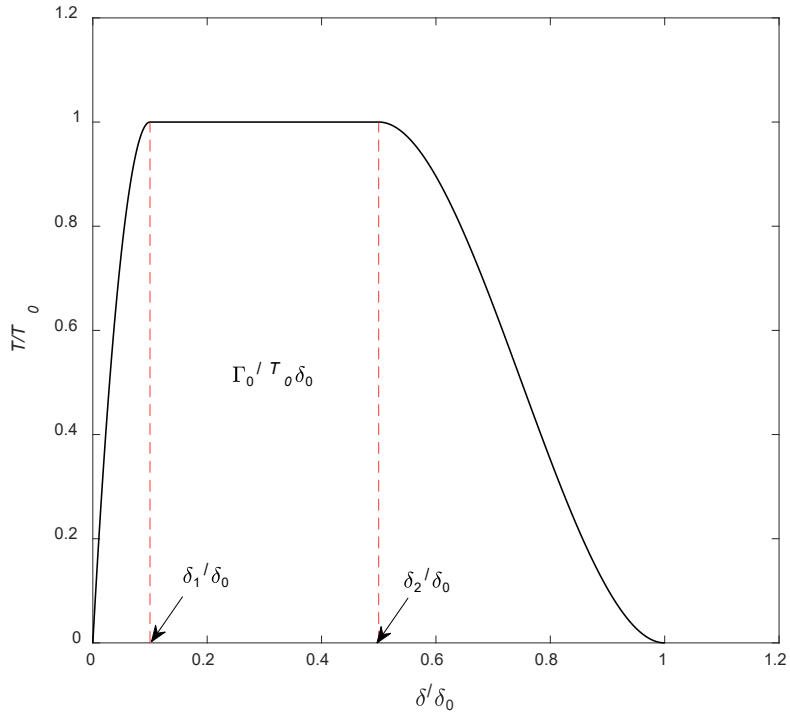

Figure 4. A schematic of the normalized smooth trapezoidal traction-separation law.

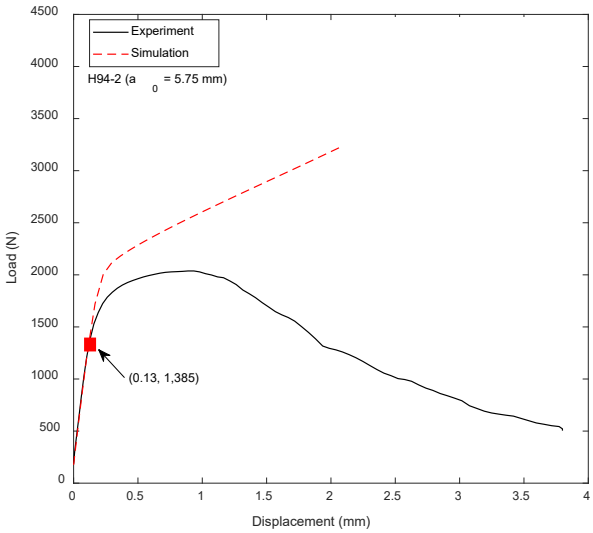

(a)

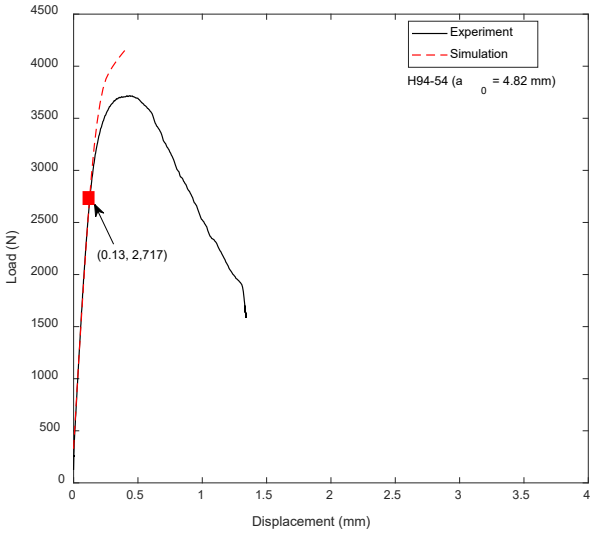

(b)

Figure 5. Comparison of the experimental load-displacement curves and the computational load-displacement curves from the finite element analyses without cohesive elements for the (a) uncharged H94-2 and (b) hydrogen-charged H94-54 specimens.

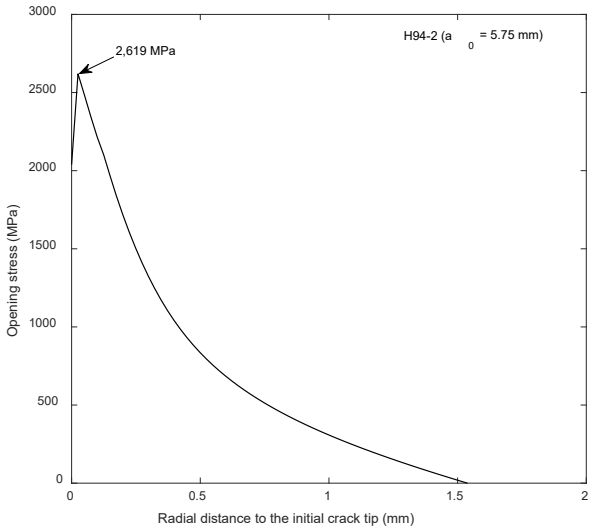

(a)

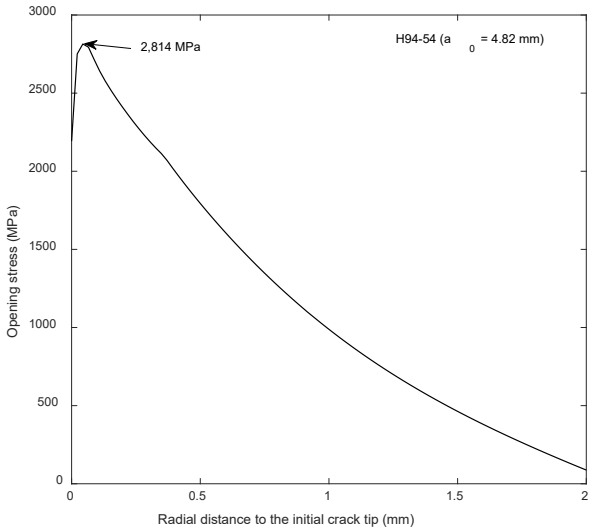

(b)

Figure 6. The distributions of the opening stresses ahead of the initial crack tips at the deviation loads for the (a) uncharged H94-2 and (b) hydrogen-charged H94-54 specimens from the finite element analyses without cohesive elements.

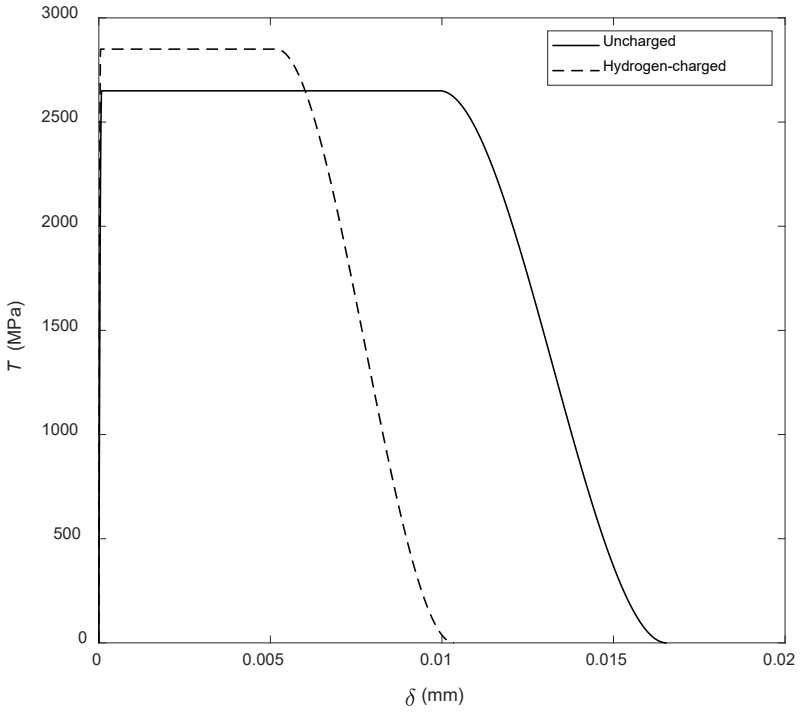

Figure 7. The smooth trapezoidal traction-separation laws for the uncharged H94-2 and hydrogen-charged H94-54 A(T) specimens.

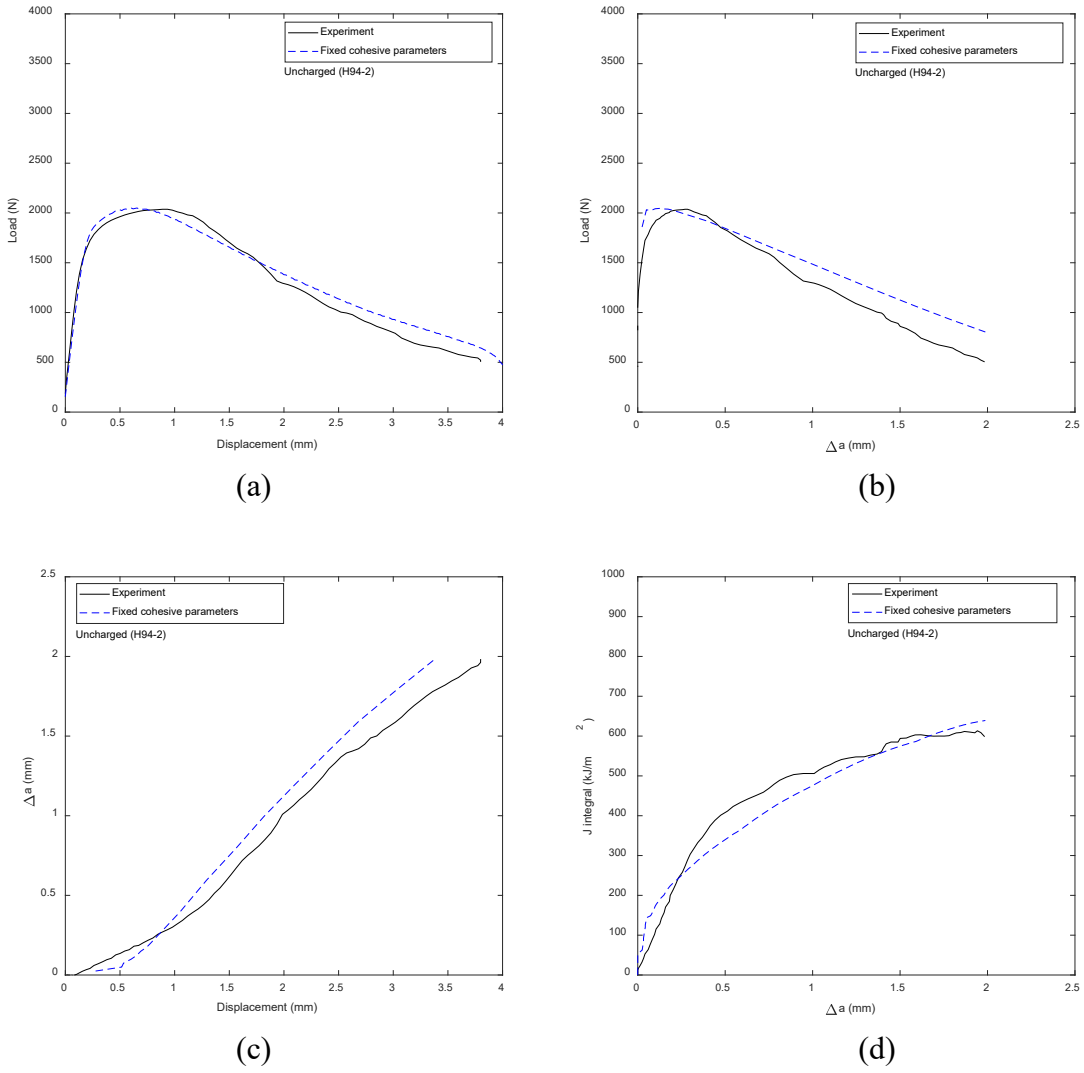

Figure 8. The computational (a) load-displacement, (b) load-crack extension, (c) crack extension-displacement and (d) J-R curves with the fixed cohesive parameters are compared with the experimental data for the uncharged H94-2 specimen.

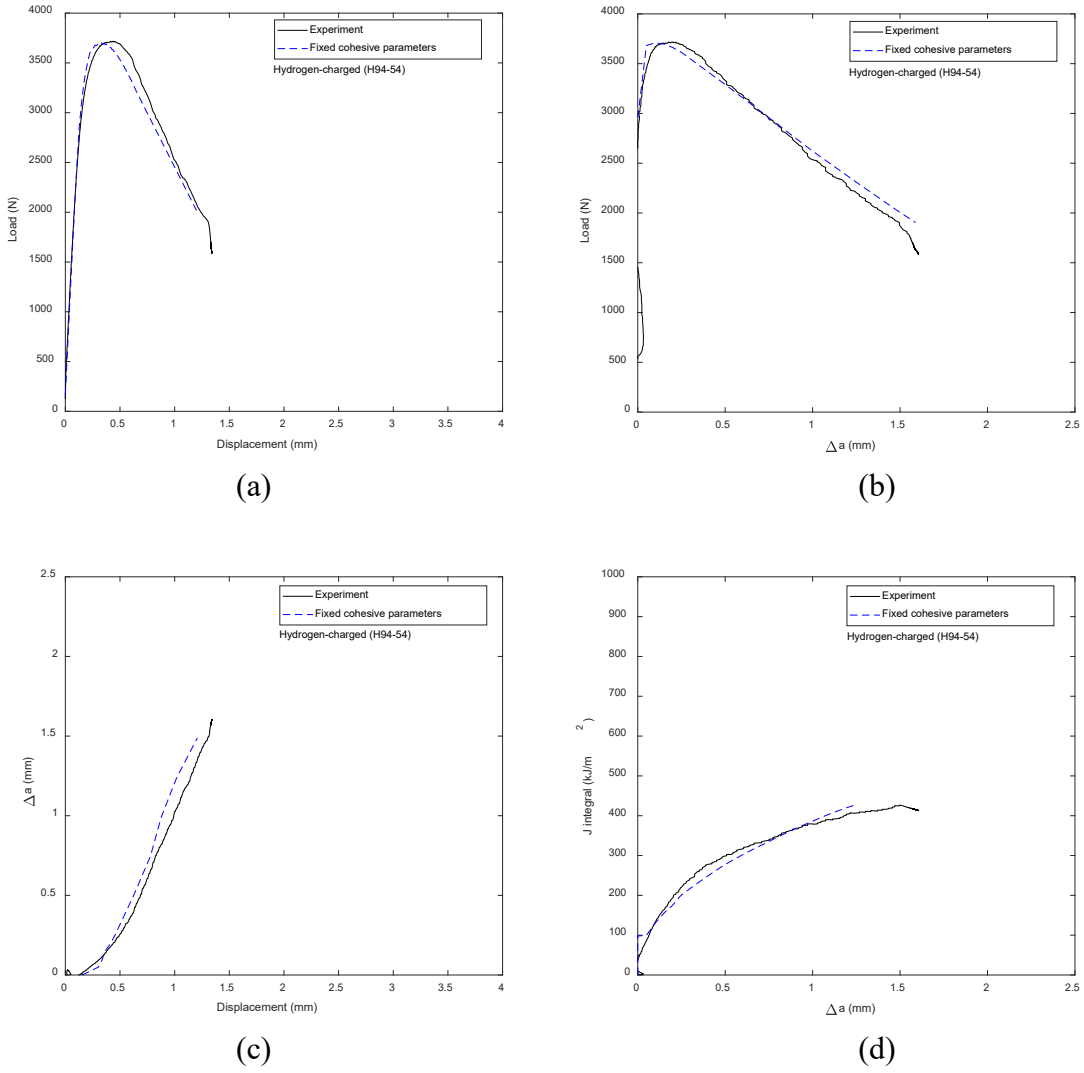

Figure 9. The computational (a) load-displacement, (b) load-crack extension, (c) crack extension-displacement and (d) J-R curves with the fixed cohesive parameters are compared with the experimental data for the hydrogen-charged H94-54 specimen.

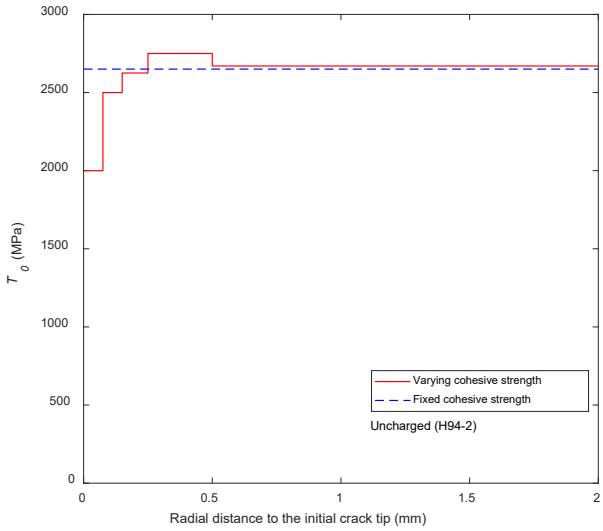

(a)

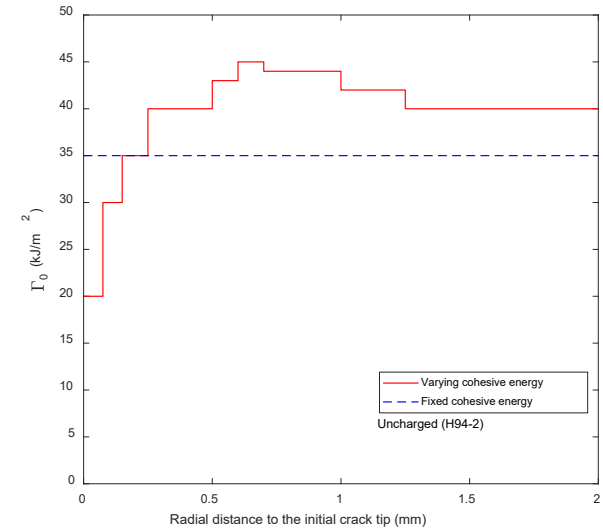

(b)

Figure 10. (a) The cohesive strength function and (b) the cohesive energy function of the radial distance to the initial crack tip for the uncharged H94-2 specimen.

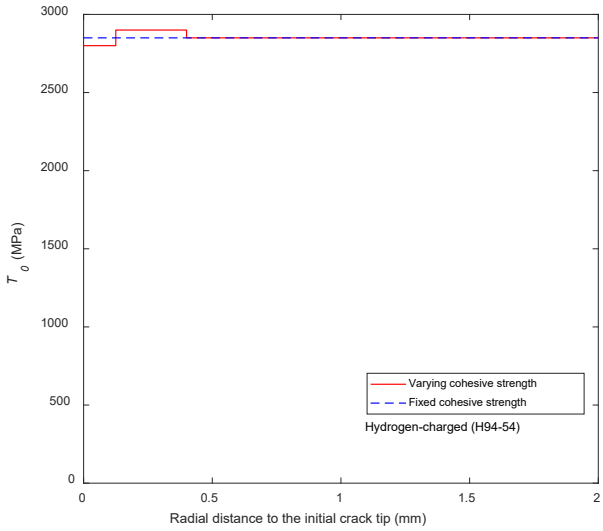

(a)

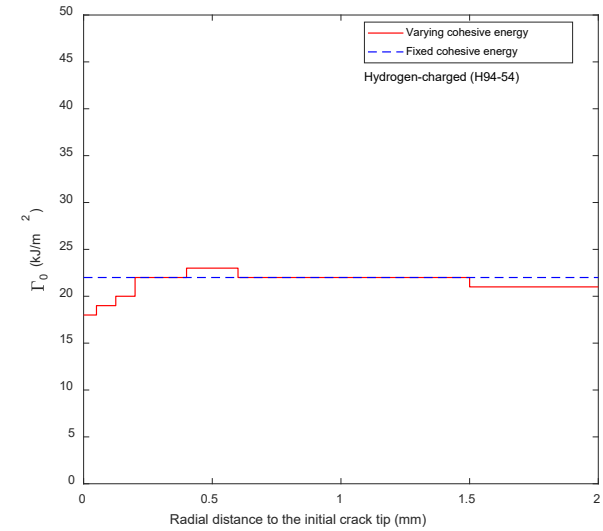

(b)

Figure 11. (a) The cohesive strength function and (b) the cohesive energy function of the radial distance to the initial crack tip for the hydrogen-charged H94-54 specimen.

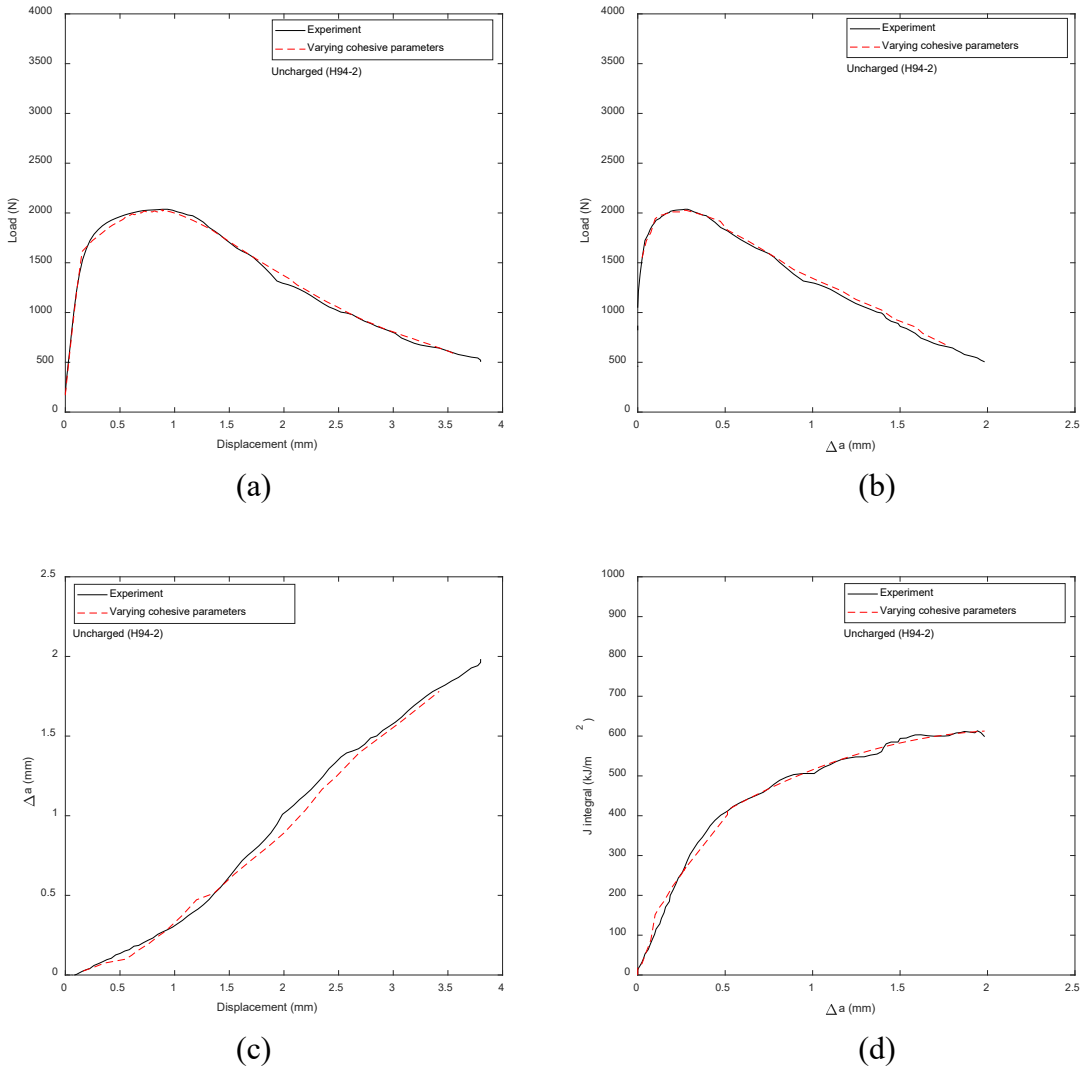

Figure 12. The computational (a) load-displacement, (b) load-crack extension, (c) crack extension-displacement and (d) J-R curves with the varying cohesive parameters are compared with the experimental data for the uncharged H94-2 specimen.

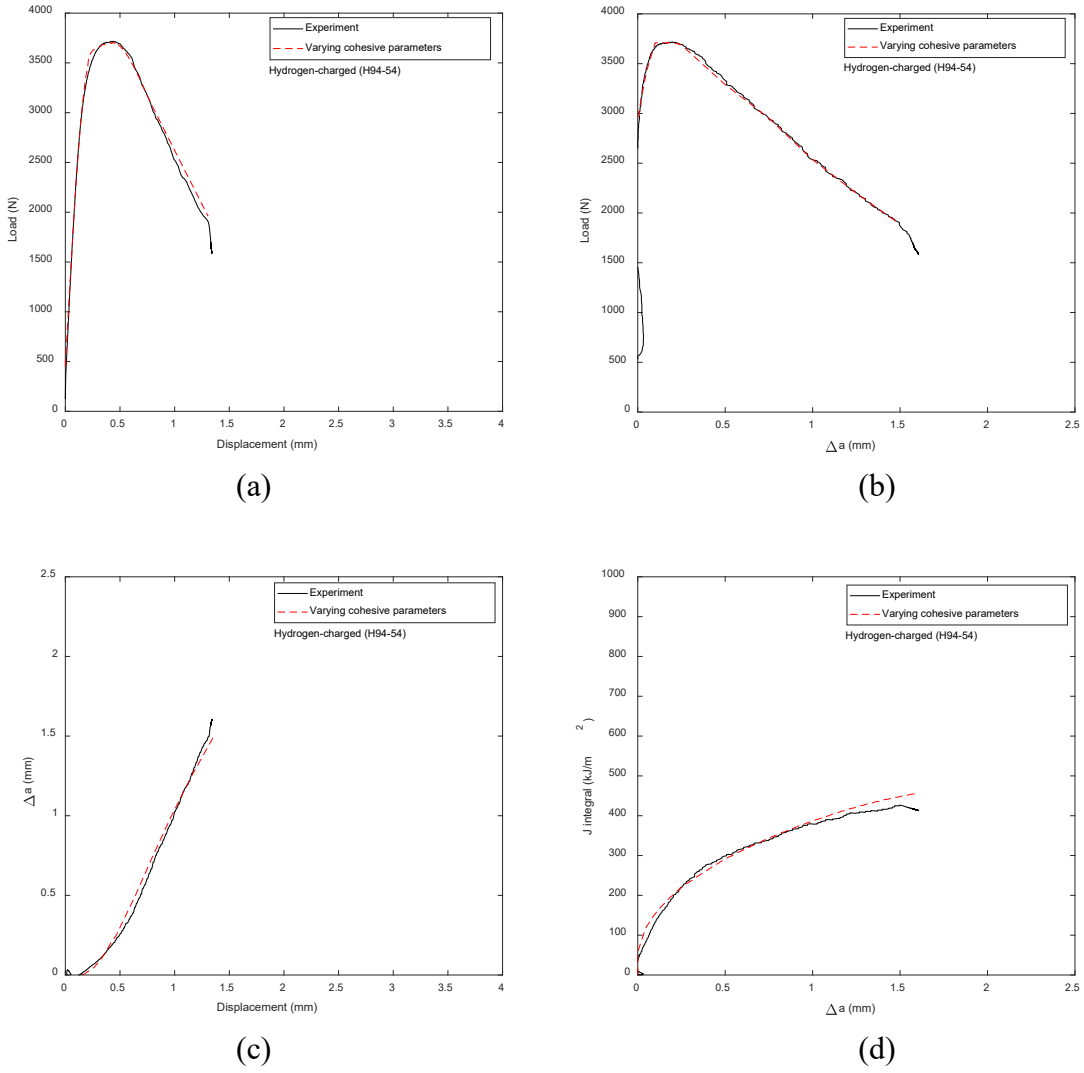

Figure 13. The computational (a) load-displacement, (b) load-crack extension, (c) crack extension-displacement and (d) J-R curves with the varying cohesive parameters are compared with the experimental data for the hydrogen-charged H94-54 specimen.

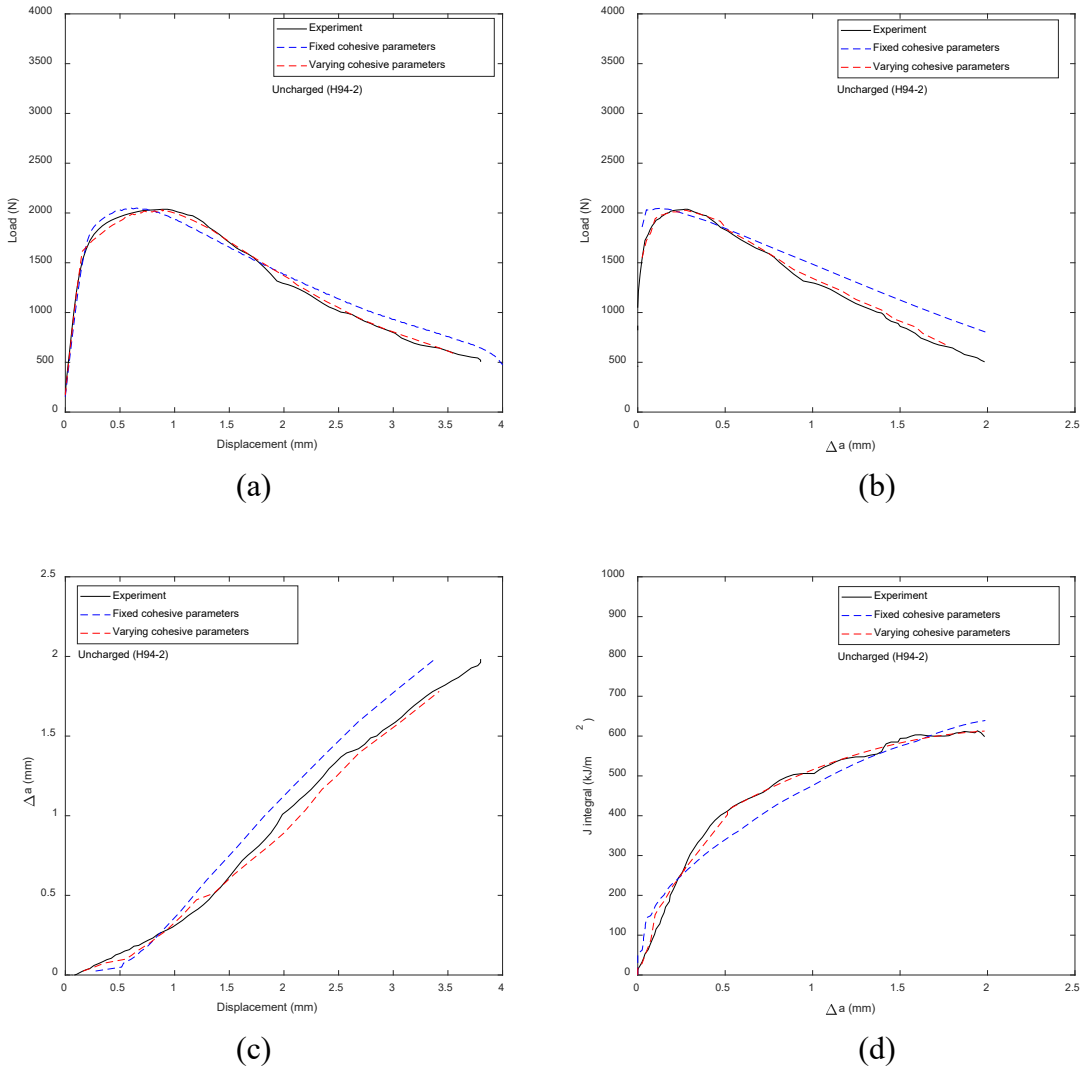

Figure 14. The computational (a) load-displacement, (b) load-crack extension, (c) crack extension-displacement and (d) J-R curves with the fixed and varying cohesive parameters are compared with the experimental data for the uncharged H94-2 specimen.

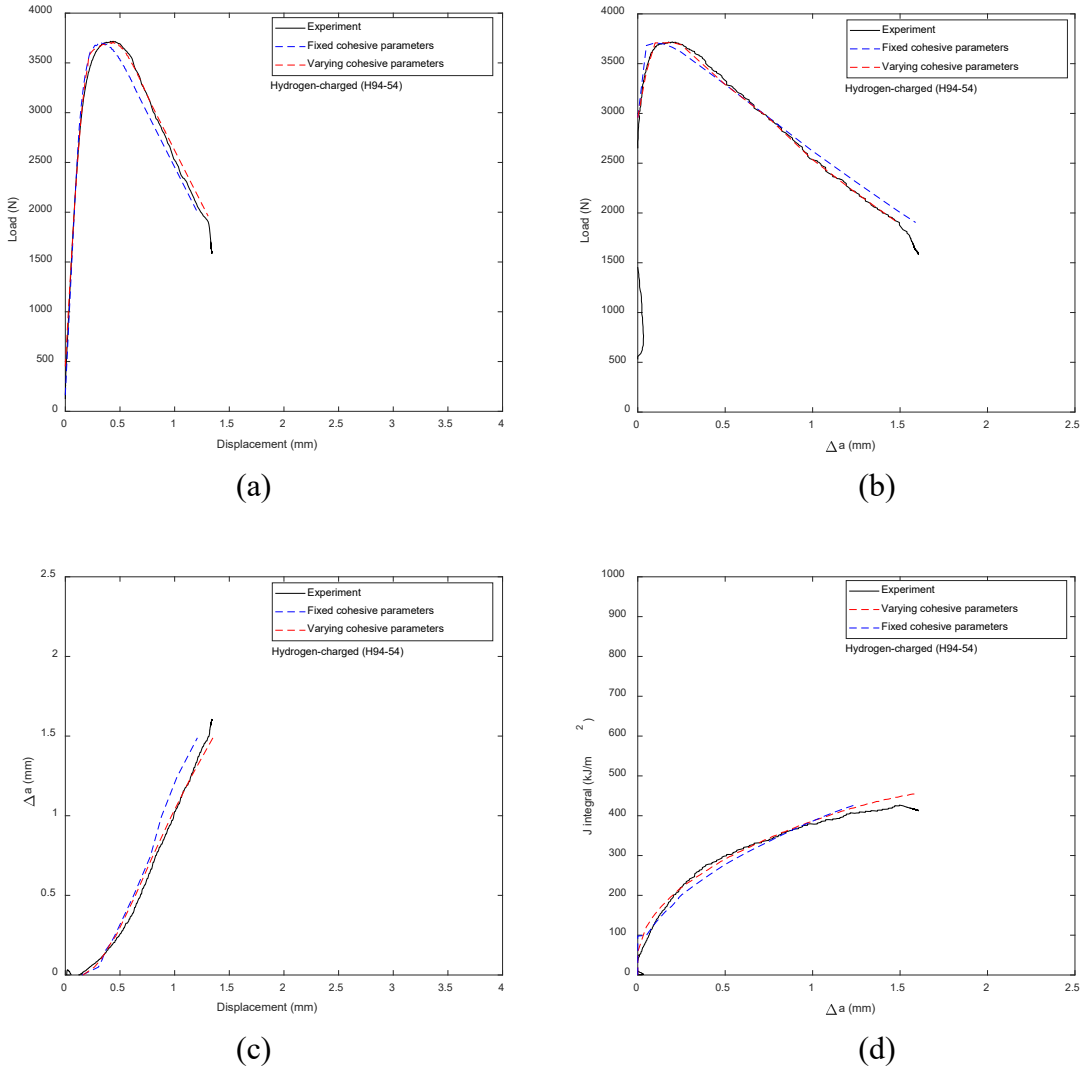

Figure 15. The computational (a) load-displacement, (b) load-crack extension, (c) crack extension-displacement and (d) J-R curves with the fixed and varying cohesive parameters are compared with the experimental data for the hydrogen-charged H94-54 specimen.

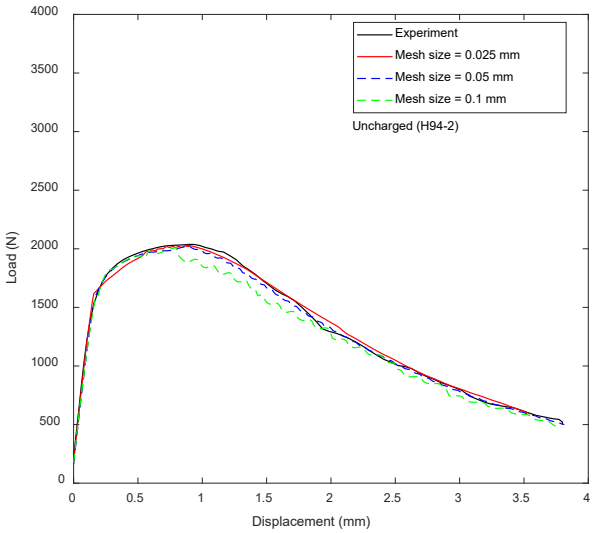

(a)

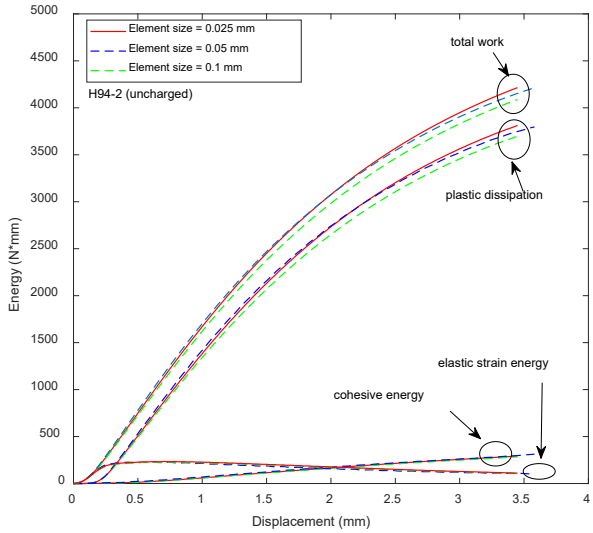

(b)

Figure 16. (a) The computational load-displacement curves for the element sizes of 0.025 mm, 0.05 mm and 0.1 mm for comparison with the experimental data and (b) the computational total work, elastic strain energy, plastic dissipation and cohesive energy as functions of the displacement for the element sizes of 0.025 mm, 0.05 mm and 0.1 mm for the uncharged H94-2 specimen.

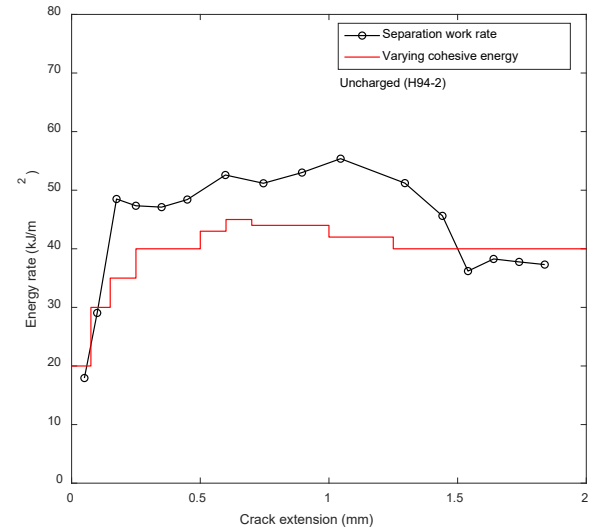

(a)

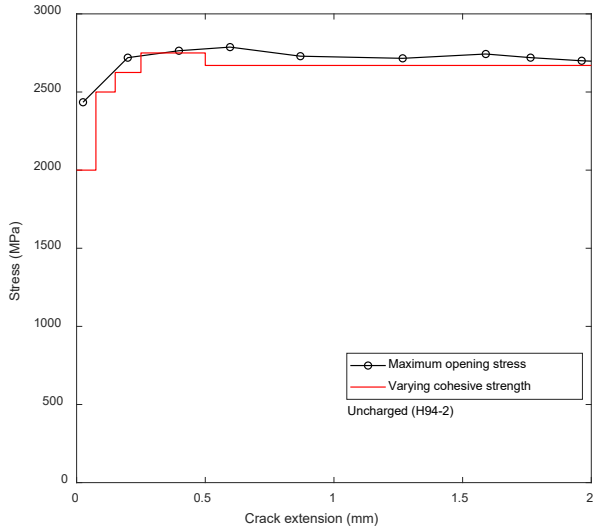

(b)

Figure 17. (a) A comparison of the separation work rate from [22] and the selected varying cohesive energy and (b) a comparison of the maximum opening stress from [22] and the selected varying cohesive strength as functions of the crack extension for the uncharged H94-2 specimen.

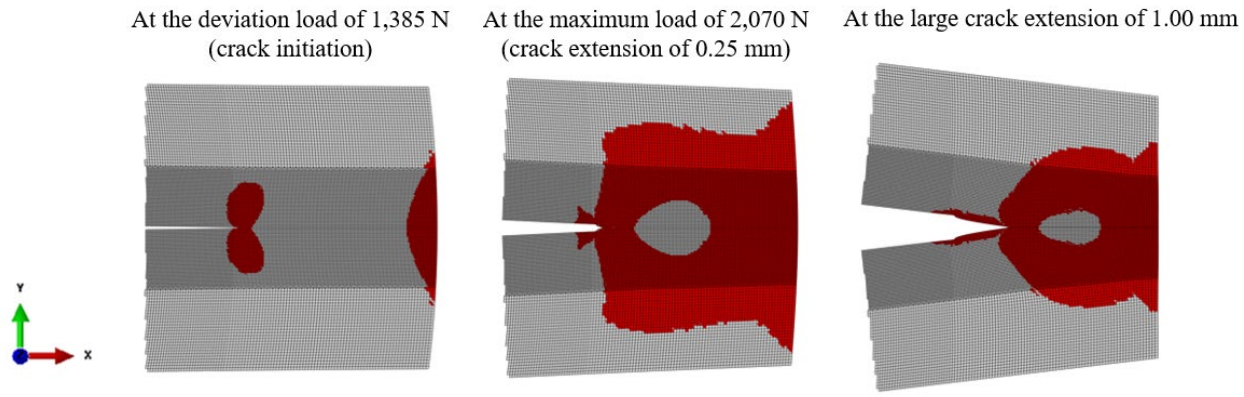

Figure 18. The plastic zone sizes and shapes in the uncharged H94-2 specimen at the deviation load of 1,385 N (crack initiation), at the maximum load of 2,070 N (crack extension of 0.25 mm), and at the large crack extension of 1.00 mm.

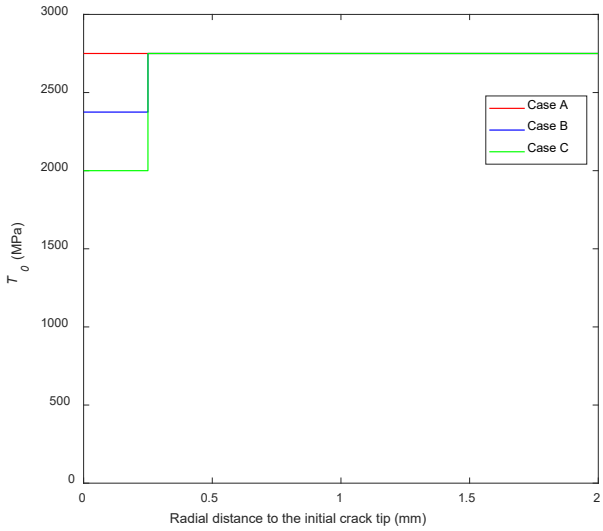

(a)

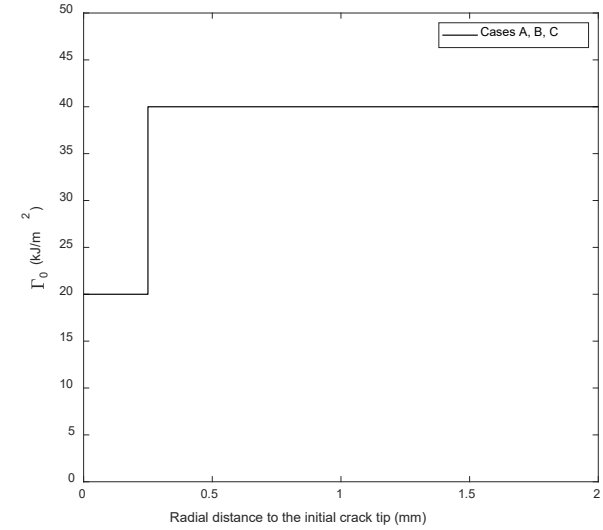

(b)

Figure A1. (a) The varying cohesive strength function and (b) the varying cohesive energy function of the radial distance to the initial crack tip for the uncharged H94-2 specimen (Cases A, B, and C).

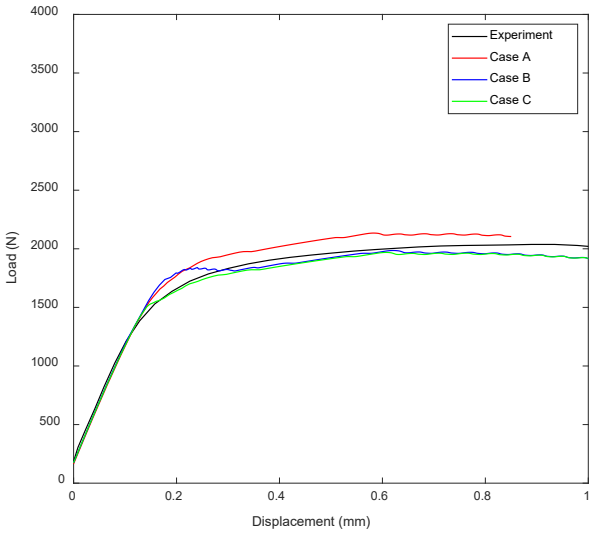

(a)

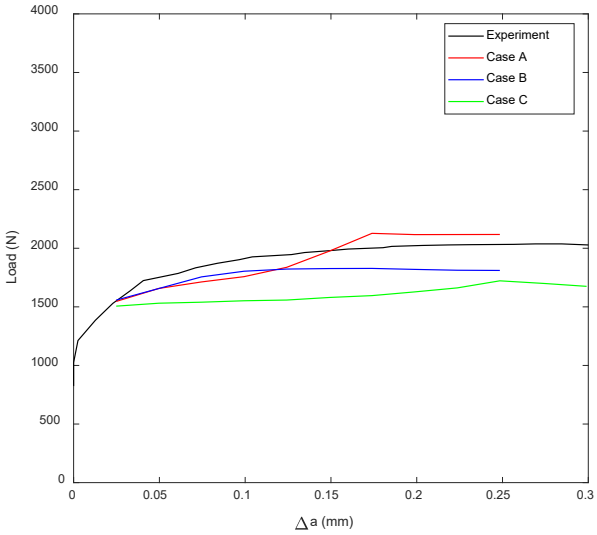

(b)

Figure A2. The computational (a) load-displacement and (b) load-crack extension curves with the varying cohesive parameters (Cases A, B, and C) are compared with the experimental data for the uncharged H94-2 specimen.

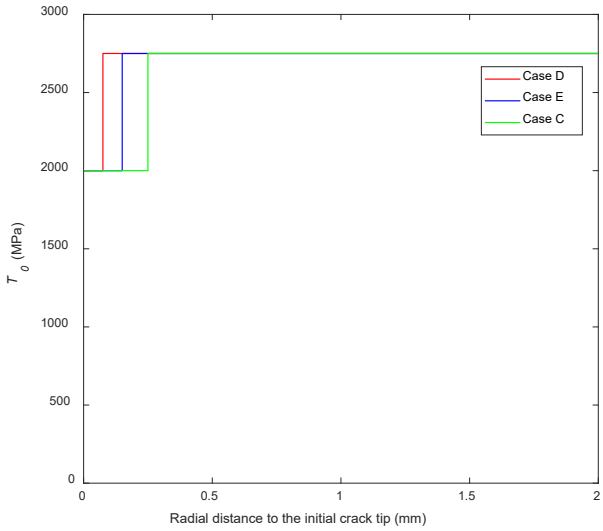

(a)

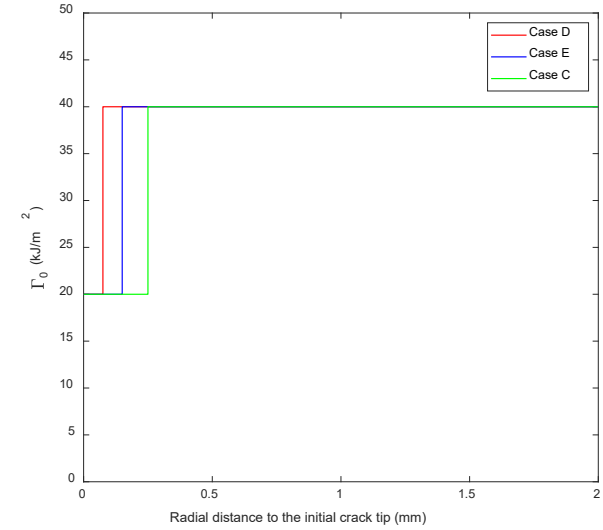

(b)

Figure A3. (a) The varying cohesive strength function and (b) the varying cohesive energy function of the radial distance to the initial crack tip for the uncharged H94-2 specimen (Cases C, D, and E).

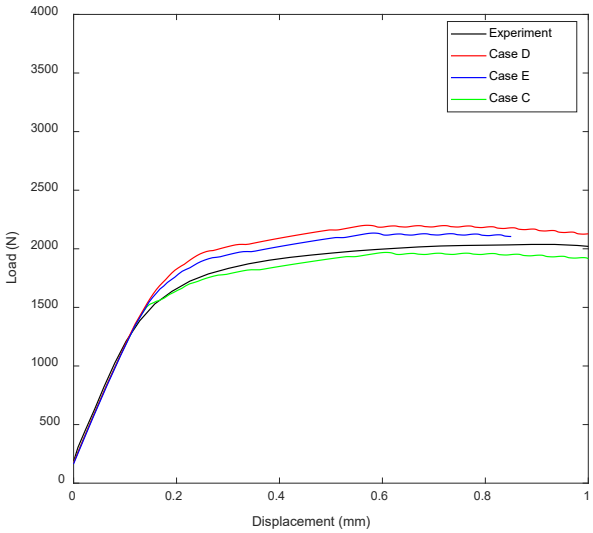

(a)

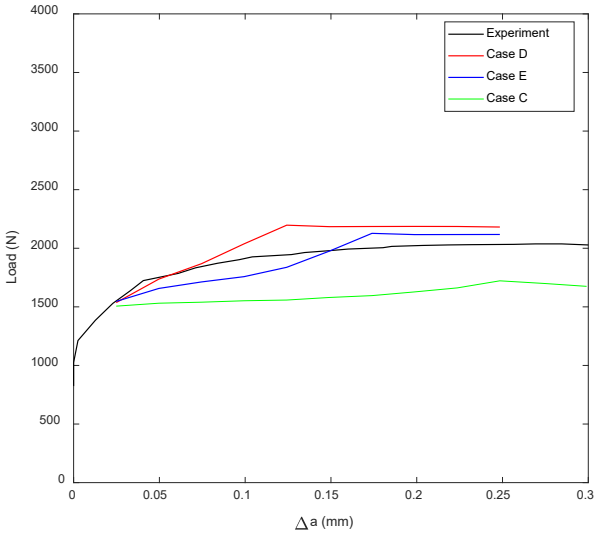

(b)

Figure A4. The computational (a) load-displacement and (b) load-crack extension curves with the varying cohesive parameters (Cases C, D, and E) are compared with the experimental data for the uncharged H94-2 specimen.

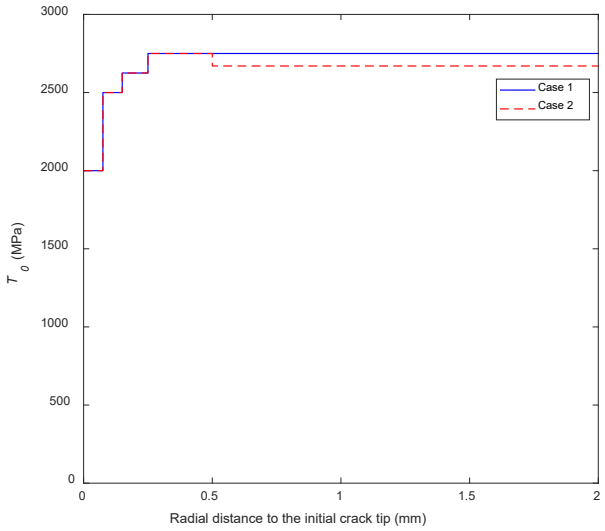

(a)

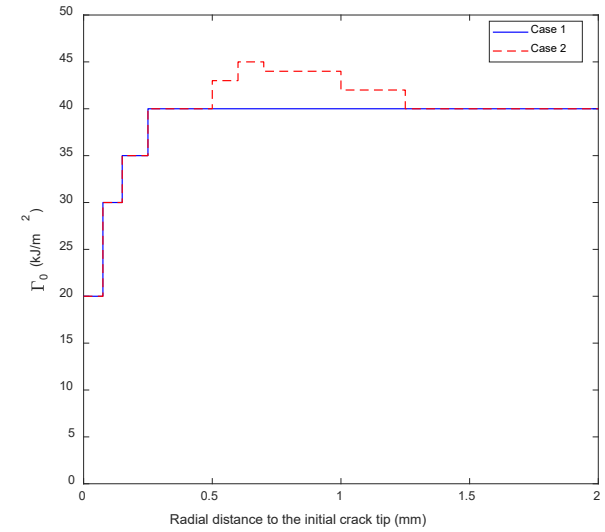

(b)

Figure A5. (a) The varying cohesive strength function and (b) the varying cohesive energy function of the radial distance to the initial crack tip for the uncharged H94-2 specimen (Cases 1 and 2).

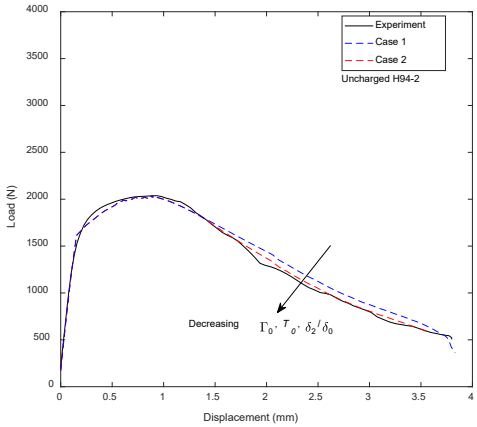

(a)

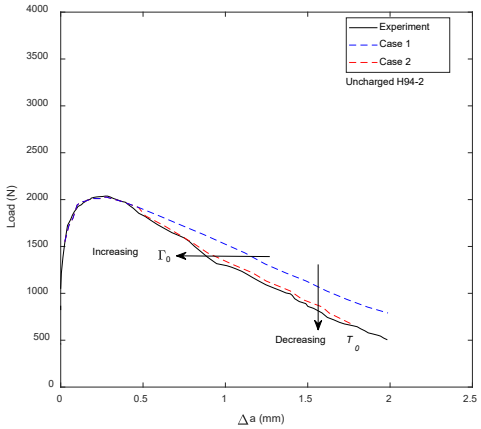

(b)

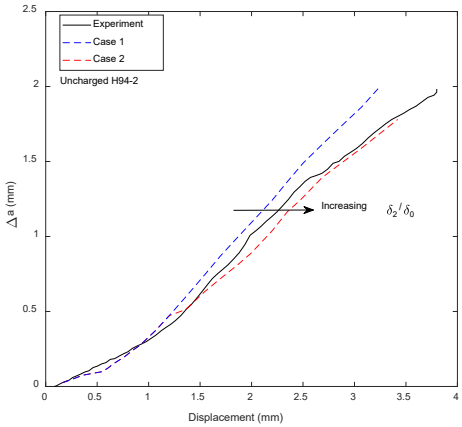

(c)

Figure A6. General trends of the cohesive parameters on the (a) load-displacement, (b) load-crack extension, and (c) crack extension-displacement curves for the uncharged H94-2 specimen.

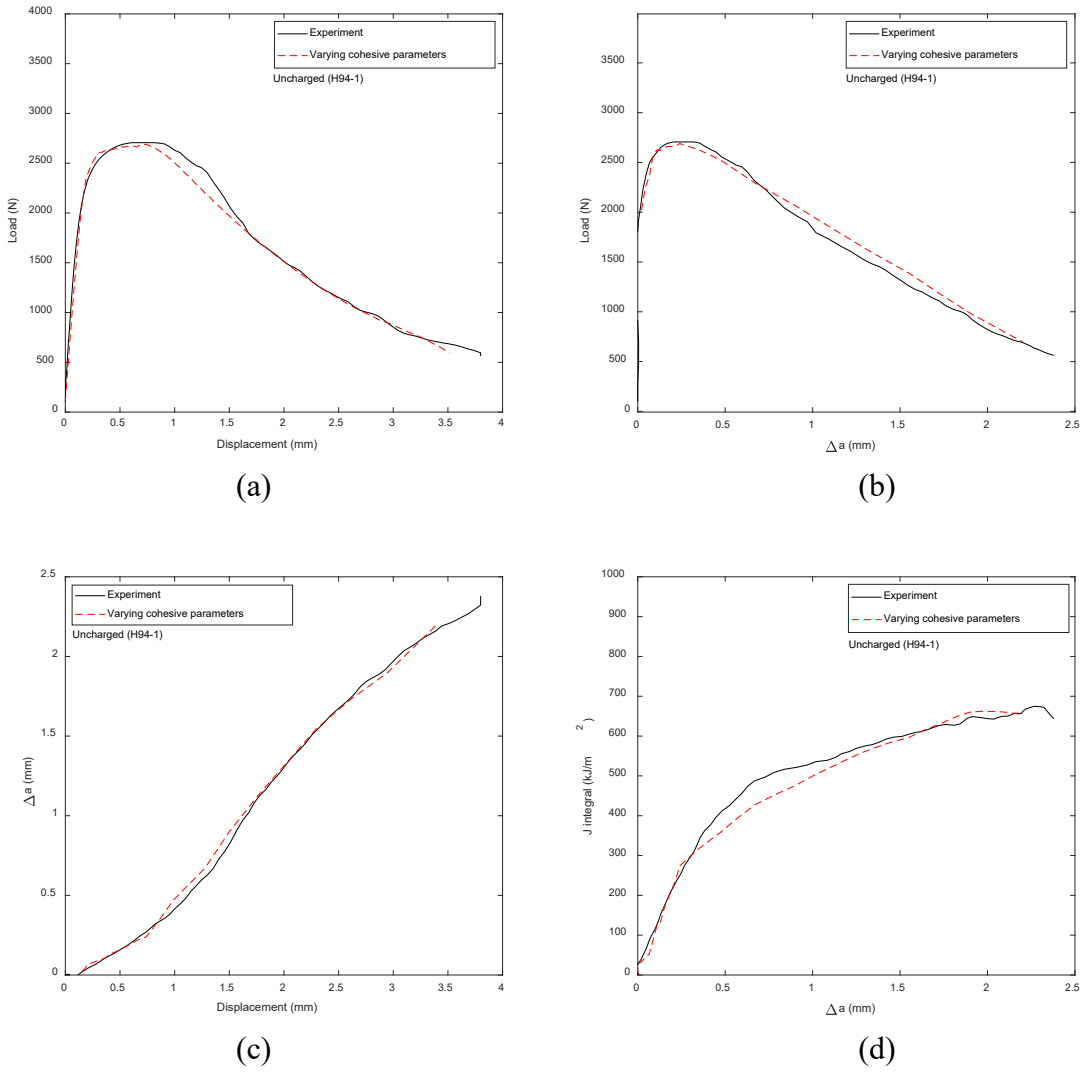

Figure B1. The computational (a) load-displacement, (b) load-crack extension, (c) crack extension-displacement and (d) J-R curves with the varying cohesive parameters are compared with the experimental data for the uncharged H94-1 specimen.

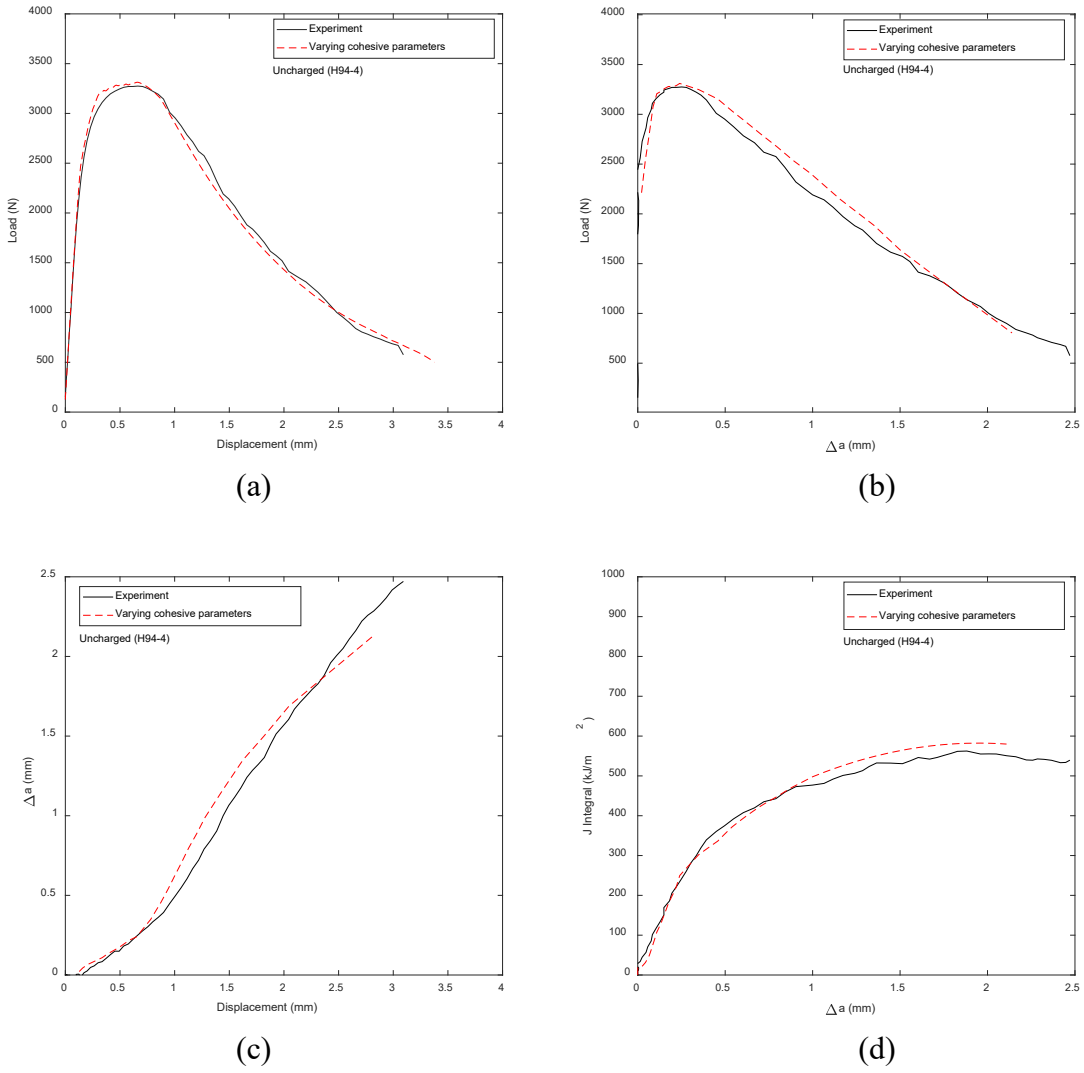

Figure B2. The computational (a) load-displacement, (b) load-crack extension, (c) crack extension-displacement and (d) J-R curves with the varying cohesive parameters are compared with the experimental data for the uncharged H94-4 specimen.